EXPERIMENTAL INVESTIGATION OF FAST PLASMA

PRODUCTION FOR THE VAIPER ANTENNA

A Dissertation
Presented to
The Academic Faculty

by

Cheong Chan

In Partial Fulfillment
of the Requirements for the Degree
Master of Science in the
Aerospace Engineering

Georgia Institute of Technology
December 2017

EXPERIMENTAL INVESTIGATION FAST PLASMA

PRODUCTION FOR THE VAIPER ANTENNA

Approved by:

Dr. Mitchell L. R. Walker, Advisor
School of Aerospace Engineering
Georgia Institute of Technology

Dr. Morris B. Cohen
School of Electrical and Computer Engineering
Georgia Institute of Technology

Dr. Wenting Sun
School of Aerospace Engineering
Georgia Institute of Technology

Date Approved: December 5, 2017

"Help young people. Help small guys. Because small guys will be big. Young people will have the seeds you bury in their minds, and when they grow up, they will change the world."

-Ma Yun (Jack Ma)

ACKNOWLEDGEMENTS

and living with you has opened a new perspective that I value. Your hard work and perseverance are exceptional. To the younger graduate students, remember to keep the music on, a steady supply of food, and caffeine in the lab. Your time as a graduate student is shorter in hindsight than you expect. Keep working hard! Tom, you have been the voice of reason and safety in the lab. I thank you for all the advice during my tenure here. To all the undergrads and soon-to-be graduate students, I thank you for all the help in the projects we worked on in HPEPL. We could not accomplish a fraction of what we have done without you. Strive to continue to become a good engineer. Everything else will naturally follow.

I would like to thank the committee members Dr. Wenting Sun and Dr. Morris Cohen. I know a professor's life is very demanding and I appreciate the time you spend to review my research. May all your grants be steady and your research have many lucky results.

Lastly, to the reader, I would like to part with these final words: this document is not the fount of truth. It is only an account of the work I have done at the end of my graduate career. Like the motto of the Royal society "Nullis in Verba," take no one's word at face value. Also, as a final note, I do not suggest eating Subway while writing a thesis; that roast beef sandwich made me feel horrible in a manner I have never felt before. Eat at your own risk.

TABLE OF CONTENTS

LIST OF TABLES

LIST OF FIGURES

LIST OF SYMBOLS AND ABBREVIATIONS

Symbol	Description	Units
B	Magnetic Field	T
C	Speed of light	$m \cdot s^{-1}$
$°C$	Celsius	°C
CF	Conflat	
e	Charge of an electron	C
E	Electric Field	$V \cdot m^{-1}$
$ft.$	feet	ft.
ϵ_0	Permittivity of free space	$F \cdot m^{-1}$
h	Planck's Constant	$m^2 \cdot kg \cdot s^{-1}$
$HPEPL$	High Power Electric Propulsion Lab	
in.	inches	in.
J	Current density	$A \cdot m^{-2}$
k_B	Boltzmann's Constant	J/k
kHz	kilohertz	kilohertz
km	kilometers	kilometers
KJLC	Kurt J Lesker Company	
LTE	Local Thermodynamic Equalibrium	
λ	wavelength	m
m_e	mass of an electron	kg
mil	1/1000 of an inch	mil
n_e	electron number density	m^{-3}
ns	nanosecond	ns
μ_0	Permeability of free space	$H \cdot m^{-1}$
PCB	Polychlorinated biphenyl	
Ω	Ohms	Ohms

$\boldsymbol{\omega_p}$	Plasma frequency	rad·s^{-1}
$\boldsymbol{V}$	Volts	volts
VAIPER	Very-short Antennas via Ionized Plasmas for Efficient Radiation	
VHF	Very High Frequency	
VLF	Very Low Frequency	

SUMMARY

Very low frequency (VLF) transmission with a frequency range from 3 to 30 kHz is used for communications and navigation due to its ability to penetrate deeply into conductors like salt water (large skin depth) and its ability to diffract around obstacles like mountains. These VLF transmissions also reflect off both the ionosphere and the earth allowing transmission to propagate far over the horizon. These features are enabled by its long wavelengths (10 to 100 km). However, traditional antennas that radiate efficiently at these long wavelengths require physical lengths of 3 to 50 km. Due to physical limitations of antenna construction, VLF radiation is usually generated with electrically-short antennas (100s of meters) that thermally dissipate a significant fraction of the input power. This inefficiency is due to the signal reflecting at the end of the electrically-short antenna and interfering with the subsequent part of the signal.

This work, Very-short Antennas via Ionized Plasmas for Efficient Radiation (VAIPER), proposes a technique to combine a fast-switching plasma and a special signal modulation scheme to circumvent the limitation of traditional antennas. The idea is to use the plasma as the conducting medium for the antenna. Plasmas allow much higher currents compared to metal conductors. By selectively turning on and off the plasma, we can suppress the reflected signal from an electrically-short antenna. In theory, this method will greatly improve the transmission efficiency of a VLF antenna of a given length. The upper frequency limit of this technique is governed by the speed that the plasma can be modulated. The challenge is to find a method to produce a plasma compatible with the VAIPER scheme that is also scalable to larger power levels.

For this Master's thesis, I will conduct the preliminary experimental study of fast plasma ignition times under varying conditions. The timing of the plasma needs to be characterized before a small scale plasma antenna can be completed. The experimental part of this project is a collaboration between Prof. Mitchell Walker's High Power Electric Propulsion Lab (*HPEPL*) in Aerospace Engineering and Prof. Morris Cohen's group in Electrical and Computer Engineering at the Georgia Institute of Technology.

CHAPTER I – INTRODUCTION

Since this area of research lies at the intersection of many disciplines not typically covered in the aerospace curriculum at Georgia Institute of Technology, a brief review of important fundamental topics is presented. In the first section, an introduction to the governing equations and characteristics of antennas will be discussed. Later, an introduction to plasma antennas and previous work done in this field will be presented. The information provided in these two sections will motivate our investigation in the Very-short Antennas via Ionized Plasmas for Efficient Radiation (VAIPER) pulsed plasma antenna scheme. A brief review of optical plasma diagnostics is presented. Lastly, we will cover the driving research questions for this thesis.

1.1 Antenna Basics

To understand the basics of antennas, we will outline the derivation of the equations describing how electromagnetic radiation is produced. In this introduction, a review of the basic governing equations of electromagnetism will be presented. It is assumed the reader is familiar with electromagnetism and we will start with a similar outline to Jackson's *Classical Electrodynamics* Chapter 9 [1].

1.1.1 *Maxwell's Equations and potentials*

To provide a brief introduction to electromagnetism, it is necessary to present first the basic governing equations. In all following discussions, letters marked in bold are vectors and we will use SI units. Maxwell's equations are the four fundamental governing equations of electromagnetism. These equations are coupled first-order partial differential

equations that describe the relationship of charges $\rho(\boldsymbol{x}, t)$ and current density $\boldsymbol{J}(\boldsymbol{x}, t)$ with the electric $\boldsymbol{E}(\boldsymbol{x}, t)$ and magnetic fields $\boldsymbol{B}(\boldsymbol{x}, t)$.

$$\nabla \cdot \boldsymbol{E} = \frac{\rho}{\epsilon_0} \tag{1}$$

$$\nabla \cdot \boldsymbol{B} = 0 \tag{2}$$

$$\nabla \times \boldsymbol{E} = -\frac{\partial \boldsymbol{B}}{\partial t} \tag{3}$$

$$\nabla \times \boldsymbol{B} = \mu_0 \left(\boldsymbol{J} + \epsilon_0 \frac{\partial \boldsymbol{E}}{\partial t} \right) \tag{4}$$

where ϵ_0 and μ_0 are the permittivity of free space and permeability of free space respectively.

One approach to solve these equations is to introduce two potentials that reduce these four equations to two second-order differential equations. They are the vector potential $\boldsymbol{A}(\boldsymbol{x}, t)$ and scalar potential $\psi(\boldsymbol{x}, t)$. The scalar potential is familiar to most who have solved basic electrostatics, but the vector potential is a more advanced concept. The electric and magnetic fields in terms of these potentials become:

$$\boldsymbol{E} = -\nabla \psi - \frac{\partial \boldsymbol{A}}{\partial t} \tag{5}$$

$$\boldsymbol{B} = \nabla \times \boldsymbol{A} \tag{6}$$

There is still a degree of freedom that will leave the equations unchanged. We will use the Lorentz gauge:

$$\nabla \cdot \boldsymbol{A} + \frac{1}{c^2} \frac{\partial \psi}{\partial t} = 0 \tag{7}$$

where c denotes the speed of light in vacuum. This choice will fix the gauge freedom.

1.1.2 *Hertzian Localized Oscillating Source*

Assume a system of charges and current density with a time-varying dependence:

$$\rho(\boldsymbol{x}, t) = \rho(\boldsymbol{x}) e^{-i\omega t} \tag{8}$$

$$\boldsymbol{J}(\boldsymbol{x}, t) = \boldsymbol{J}(\boldsymbol{x}) e^{-i\omega t} \tag{9}$$

It is also assumed that these sources are in vacuum. In the Lorentz gauge, the solution to the vector potential as a function of the current is:

$$\boldsymbol{A}(\boldsymbol{x}, t) = \frac{\mu_0}{4\pi} \int d^3 x' \int dt' \frac{\boldsymbol{J}(\boldsymbol{x}', t)}{|\boldsymbol{x} - \boldsymbol{x}'|} \delta\left(t' + \frac{|\boldsymbol{x} - \boldsymbol{x}'|}{c} - t\right) \tag{10}$$

Inserting the current density into the previous equation and evaluating the time integral with the delta function.

$$\boldsymbol{A}(\boldsymbol{x}) = \frac{\mu_0}{4\pi} \int \frac{\boldsymbol{J}(\boldsymbol{x}')\, e^{\frac{i\omega|\boldsymbol{x} - \boldsymbol{x}'|}{c}}}{|\boldsymbol{x} - \boldsymbol{x}'|} d^3 x' \tag{11}$$

Using the equations presented in the previous subsection, we can solve the electric and magnetic fields. If we assume the current distribution is small compared to the wavelength of radiation and we are far from the source, we can expand equation 11 in terms of powers of k (where $k = \omega/c$ is the wave number). Since we are interested in only the first term that goes as $1/r$, the vector potential becomes:

$$\boldsymbol{A}(\boldsymbol{x}) = \frac{\mu_0}{4\pi} \frac{e^{ikr}}{r} \int \boldsymbol{J}(\boldsymbol{x}')\, d^3 x' \tag{12}$$

With this equation and the equations for the electric and magnetic field, it is possible to calculate the total power radiated from a dipole. Assuming a center-fed dipole with a length $d << \lambda$ (the wavelength of the oscillation) and the currents fall linearly away from the center to zero at the edges (with a center value of I_0), it is possible to show the total radiated power P is:

$$P = \frac{Z_0}{48} \frac{I_0^2}{\pi^2} (kd)^2 \tag{13}$$

where $Z_0 = \sqrt{\mu_0/\epsilon_0}$ is the impedance of free space. It is clear from this expression that, for a traditional dipole antenna to radiate efficiently, the radiating source should be of the order the size of the wavelength. Additionally, larger currents will generate more transmitted power.

1.2 Plasma Antenna Review

To improve beyond the performance of fixed form-factor metal antennas, researchers started to look at antennas whose conducting medium is composed of plasma [2-7]. A plasma is a quasi-neutral (on average equal number of positive and negative charges) cloud of positively, negatively, and neutrally charged particles. The conductivity of a plasma can be changed by controlling the discharge conditions (applied voltage, applied current, gas composition, etc). This ability to control the antenna offers many benefits discussed later. While there are many characteristics that characterize a plasma, the most important parameter for a plasma antenna is the plasma frequency

(ω_p):

$$\omega_p^2 = \frac{n_e\, e^2}{\varepsilon_0\, m_e} \tag{14}$$

where m_e is the mass of the electron, e is the charge of the electron, n_e is the electron number density and ε_0 is the permittivity of free space. This is the most fundamental time scale of a plasma and represents the fastest time a plasma can react to an external excitation. Below this frequency, the plasma will act like a conductor where electrons have enough time to move and cancel the field in the bulk. An entering electric wave will damp exponentially as it enters the plasma if the plasma frequency is greater than the incident wave frequency.
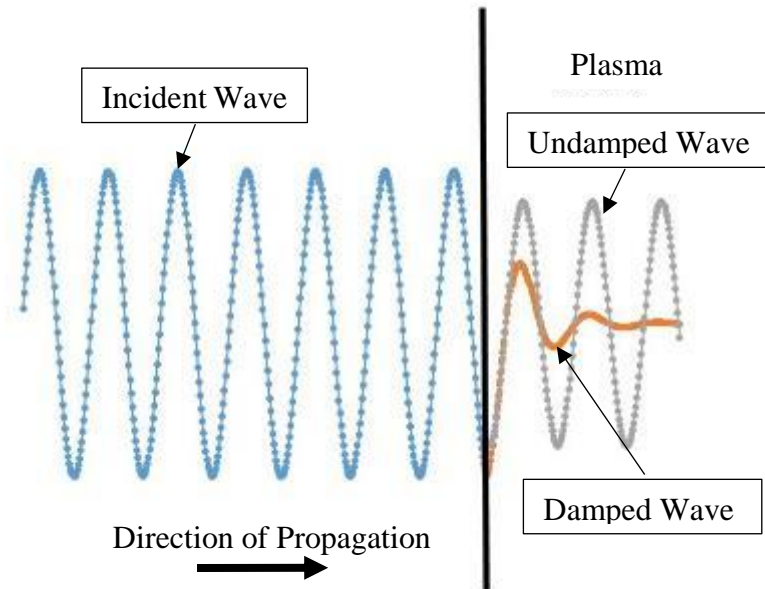
FIGURE 1 – Diagram depicts an electromagnetic wave entering an ideal plasma. The blue wave represents an incoming wave into the plasma. The orange wave represents the resultant wave if the plasma frequency is greater than the wave frequency. The gray represents the resultant wave if the plasma frequency is lower than the wave frequency.

Waves with greater frequency than the plasma frequency will pass through the plasma with reduced amplitude. The electrons cannot move fast enough to fully cancel the

effect of the field propagating in the plasma. These two limiting cases are diagrammed in Figure 1. Additional details about plasma generation will be given in the next chapter.

Anderson and Alexeff previously worked with fluorescent and neon tubes to produce plasma antennas [2-5]. For these researchers, the benefits of plasma antennas were reduced radar cross-section and reconfigurable arrays. By turning off the plasma, the tube is filled with a non-conductive gas that will not reflect radar signals. Selectively turning off individual tubes in an array can be used to open transmitting windows. With short, direct current (DC) pulses, they demonstrated turn-on times of 2 µs. The turn-off times were on the order of 10 ms. The plasma density was considerably higher in pulsed mode discharges compared to their previous studies with DC discharges (4 x 10^{10} cm^{-3} and 6.4 x 10^9 cm^{-3}, respectively). The boundary of frequencies of electromagnetic waves that see the plasma as a conductor scales with the square root of n_e. They tested the antenna transmission frequency from 30 MHz to 20 GHz. Additionally, the noise measured due to the plasma antenna was only a few decibels above that of their metal analogs. Figure 2 depicts one of the plasma antenna that Alexeff et al. studied [4].

FIGURE 2 – Picture of a plasma antenna made from a neon tube [4].

In summary, these previous studies show that plasma antennas are viable for a wide range of frequencies above VHF, but their configurations in these studies do not offer considerable performance improvements in comparison to their metal analogs. In the next section, we will discuss a new method to use plasma antennas for radio transmission that will offer significant performance improvements.

1.3   Pulsed Plasma Antenna Scheme

This section presents the Very-short Antennas via Ionized Plasmas for Efficient Radiation (VAIPER) scheme. This antenna consists of plasma cell sections whose conductivity is modulated by turning the plasma in these cells on and off. At the same time, a low-frequency signal from a function generator is modulated with a higher frequency (GHz range) amplitude modulation. This modulated signal is then fed into the antenna. The signal pulses will propagate down to the end of the antenna and reflect. As the signal pulse

reflects, the plasma at the end segment will turn off and dissipate the reflected signal. Removal of the conducting medium from the downstream end of the antenna prevents the interference problem experienced with traditional metal antennas. This process is illustrated in Figure 3.
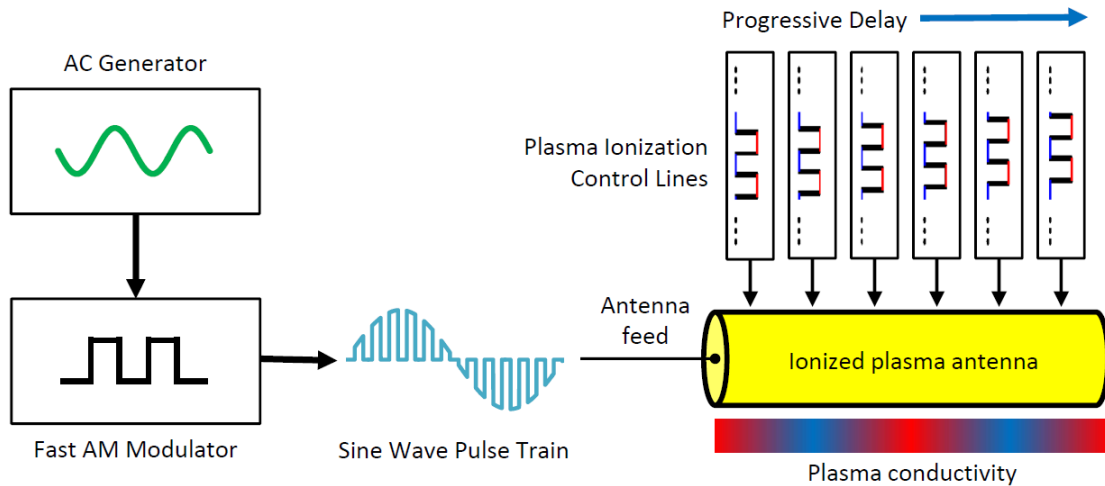
FIGURE 3 – Diagram of the VAIPER scheme of signal input on the left and the plasma antenna with modulating sections on the right.

Since this matching technique is performed in the time domain, the maximum operational frequency depends on the speed that you can modulate the plasma conductivity. Techniques to modulate the original signal into a pulse train exist and can be achieved with commercially available switches that have transitions times less than 2 ns. Our approach applies towards the VLF regime where the antennas are electrically small due to construction/cost constraints.

While the electronics for the signal modulation exists, the technique to generate and modulate the plasma is an open area of research that we will begin to investigate in this thesis. The challenge comes from the need for fast rise time and fast de-ionization

(quenching) time of the plasma for the scheme to work. This must be on the order of a nanosecond since the signal propagation speed is near the speed of light. While it is possible to turn on plasmas on this time scale, the quenching (fast reduction in conductivity) is more difficult. The slow quenching time can lead the need to increase the length of the VAIPER plasma antenna cells. This is illustrated in the significant difference in time for the previous plasma antenna experiments [4].

1.4   Optical Plasma Diagnostics Review

The plasma under investigation is small in dimensions compared to typical probes constructed in HPEPL. Perturbations due to the presence of the probe, arcing and the electrical noise picked up by an electrical probe inserted into a pulsed plasma make direct measurements of plasma parameters difficult. To circumvent these issues, the plasma in this experiment will be investigated using optical diagnostics [8-10]. This chapter details various optical plasma diagnostics and expands on the background of the methods we wish to employ in this thesis.

1.4.1   Active Optical Methods

The main methods of active optical diagnostics can be divided into two groups of observations: how a controlled electromagnetic source interacts with ions or neutral atoms in the plasma and how a controlled electromagnetic source interacts with free electrons in the plasma. This section contains an overview of these methods.

1.4.1.1 Active Spectroscopy

The study of how a known electromagnetic source interacts with the bound electrons in the ions and neutral atoms in the plasma is considered absorption spectroscopy. This form of spectroscopy requires knowledge of the species under test and a well-characterized light source.

This light source can be an incoherent light source such as a xenon arc lamp or LEDs [11-14]. To measure the absorption signal of a transition line in the plasma, alternate spectra of the plasma with a backlit source and spectra with the plasma only are taken. The difference between the two sets of spectra compared to the spectra of the incoherent source results in the transmittance of the plasma along the line of integration. Physical dimensions, knowledge of the transition and assumptions about the homogeneity of the plasma allow for an estimation of plasma properties. Alternatively, as lasers have become more compact to incorporate into experiments, their use have become more popular in absorption spectroscopy [15-17].

1.4.1.2 Electron Interactions

Since the electron and ions are a charged particles and photons are electromagnetic wave packets, it is also natural to expect to be able to obtain a signal from the change of a non-resonant electromagnetic field (i.e., a frequency that does not correspond to an atomic transition) propagating in plasma. The two main methods of characterizing a plasma using a coherent non-resonant source are Thomson scattering and interferometry.

Thomson scattering occurs when a charged particle accelerates in the electric field of an incident photon. This effect is considered an elastic scattering since the particle kinetic energy and photon energy are conserved. Thomson scattering limit as valid if the

photon energy is much less than the rest mass energy of the particle. Otherwise, as the photon energy becomes comparable to the rest mass energy of the particle, different physical processes (radiation-pressure recoil and Doppler shift of scattered light) become significant [18]. Compton won the 1927 Nobel Prize in Physics for his observations showing light should be treated as quanta (called photons). In the application to plasma diagnostics, a laser beam propagates through a region of the plasma under test. The electron density is determined from the intensity of the scattered light [19-22].

When an electromagnetic wave travels through a plasma, its propagation speed is slower than its speed in air. This phase shift is inversely proportional to the wavelength of the electromagnetic wave and proportional to the plasma density integrated along the path of the laser beam propagation through the plasma. In plasma diagnostics, this phase shift measurement typically employs microwaves [23-26]. More recently, interferometry has also been performed using other wavelengths for plasma diagnostics [27, 28].

1.4.2 **Passive Optical Methods**

Due to the time required to setup and verify an active optical method, this work focuses on more readily available passive optical methods at HPEPL that allow us to do some preliminary characterization of the plasma while the active methods are concurrently being developed.

1.4.2.1 Optical Emission Spectroscopy

If local thermodynamic equilibrium (LTE) is satisfied, the temperature determines the population distribution among the energy levels of the atom. The analytic expression

that describes this population distribution is the Boltzmann equation. Additionally, the Saha equation describes the ionization equilibrium among the ionization states of the atom. In this work, we assume partial LTE exists in order to determine various plasma parameters. Partial LTE assumes the atomic levels can still be described with a Boltzmann distribution with an excitation temperature T_{exc}. This excitation temperature and the electron temperature are assumed to be the same in this equilibrium. This approach has been applied to laser-induced plasmas whose time scales are $\sim$ 100 ns to 10 µs [30, 31]. We also assume the plasma is optically thin and the absorption is negligible.

The combination of the Boltzmann equation and the emission irradiance with some manipulation results in the following equation:

$$\ln\left(\frac{g_i A_{ij} c}{I_{ij}\, \lambda_{ij}}\right) = -\frac{E_i}{k_B T_{exc}} + \ln\left(\frac{4\pi g_0}{hlN_0}\right). \tag{15}$$

Here, E_i is the energy and g_i statistical weight of the excited state i. I_{ij} and λ_{ij} is the emission radiance and wavelength of the transition between states i and j. The physical constants are the speed of light c, Boltzmann's constant k_B and Planck's constant h. In the second term on the right side of equation 15, l is the plasma thickness (assumed to be constant). N_0 and g_0 represent the ground state population and statistical weight. Due to the difficulty of absolute calibration, we opt instead to use relative intensities in our study. This results in an additional constant factor on the right side since all the transitions used to create the Boltzmann plots have the same intensity normalization. In some studies, an additional correction factor in used to account for non-equilibrium effects that are also neglected in this work. The most important factor we want to extract is the excitation temperature T_{exc}.

This value is obtained by the slope of the left hand factor and the energy of the upper level E_i.

With the partial LTE assumption, the excitation temperature T_{exc} and the electron temperature T_e are equal. Thus, once the excitation temperature has been determined using the Boltzmann plot, an estimate of the electron density can be made using a commercial plasma software package PrismSPECT. This software package will be described later.

1.5 Research Questions

Before the VAIPER collaboration can make a full-scale antenna, several questions about the method of plasma production must be answered. The chief among them are: At what speed can we initiate a plasma and what is the quality of the plasma produced in this process? For this Master's thesis, I will conduct the preliminary experimental study of fast plasma ignition under varying conditions using the optical and electronic diagnostics.

1.5.1 Plasma Rise Time Measurement

Additionally, the plasma must switch quickly (~1 ns) or the VAIPER antenna will need to increase in length to compensate. As the time for the plasma to reach a critical electron density depends on the gas conditions and discharge inputs, we will investigate fast plasma generation using a pulsed DC capacitively-coupled discharge at various pressures of argon (1 and 2 Torr) and pulse repetition frequencies (1 kHz, 5 kHz, 10 kHz, 25 kHz, and 50 kHz) at 1 kV discharge voltage. Since we do not have any active methods to detect the electron density directly we will use the light emission from the plasma as a proxy to limit the rise time of the plasma. Specifically, we will use a fast avalanche

photodiode detailed later to detect the rise time of the light curve during a plasma pulse. Since plasma ignition is typically dominated by collisional excitation and radiative or collisional de-excitation, the amount of light emitted by the discharge volume is proportional to the number of electrons.

1.5.2 *Optical Plasma Characterization*

A critical qualification for fast plasma generation is the ability to reach a critical electron number density such that the plasma will act as a conductor for our signal pulse train used for the VAIPER scheme. If we cannot achieve this number, the VAIPER antenna will not work. To characterize this plasma, we will obtain spectra of the plasma using the experimental setup detailed in the next chapter. We will use the same settings as the rise time measurement (argon pressures of 1 and 2 Torr and pulse repetition frequencies 1 kHz, 5 kHz, 10 kHz, 25 kHz, and 50 kHz at 1 kV discharge voltage). From the various discharge conditions combined with the assumptions and analysis detailed in the optical emission spectroscopy section should yield an estimate of the electron temperature. From this electron temperature, it is possible to calculate an estimate electron number density.

CHAPTER II – EXPERIMENTAL APPARATUS

This setup has evolved quite a bit since the initial prototype setup. The first major section details where the setup began and the problems encountered with the design. Using the lessons learned from each improvement, we detail the finalized setup and the logic motivating the design used for the measurements in this thesis.

2.1 Initial Prototype Setup

To study a suitable plasma generation method for the VAIPER antenna scheme, the group decided to build a single cell of the plasma antenna first. The group would then build a larger antenna with multiple plasma cells to determine antenna performance properties after the single plasma cell design has been determined to be successful and scalable. This effort runs in parallel to a modeling effort made by our collaborators at University of Colorado, Denver and Tech-X Corp.

As the goal of this type of plasma generation is unique, it was decided the prototype cell setup would need to be quickly reconfigurable for both changes in discharge methods and diagnostics. The resulting initial prototype cell is depicted in a Solidworks model in Figure 4.
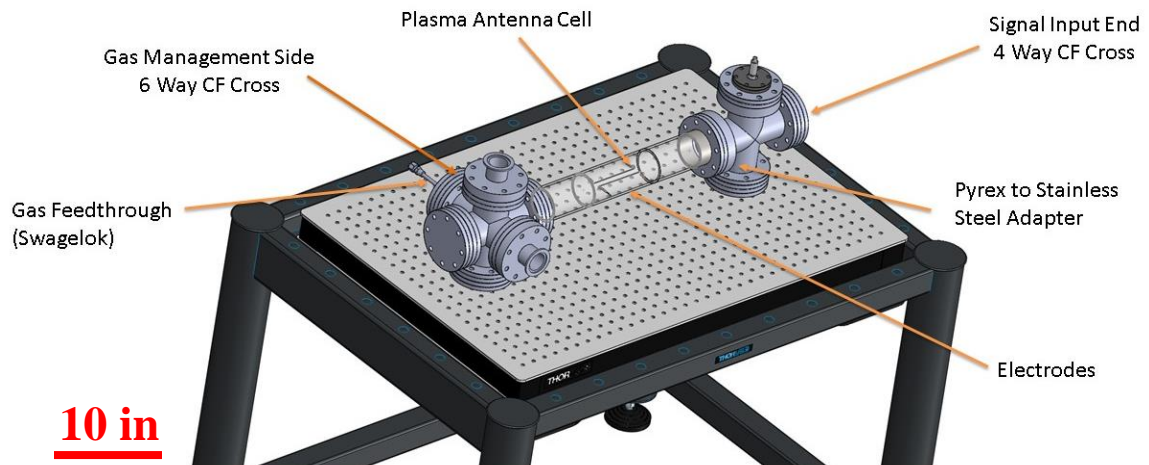
FIGURE 4 – Diagram depicts a rendering of the main parts of the experimental setup of the prototype plasma cell. The Thorlabs optical table is 3 ft. by 4 ft. in size.

2.1.1 Initial Plasma Cell

This initial plasma cell setup used a single pair of aluminum electrodes made from sheet metal to create a simple plasma discharge. The DC high voltage was supplied by a Lambda GEN600-2.6 power supply (Max 600 V, 2.6 A). The 6-way and 4-way crosses on the sides of the middle glass tube are stainless steel with 4.5 in Conflat (CF) flange connections. This was used to ensure good sealing (CF flanges rated up to 10-13 Torr) on ports that are rarely changed and good thermal conductivity in case we decide to dissipate more power in the glass plasma cell. The crosses also provide many access points for the gas feedlines, a vacuum pump, electrical feedthroughs, and a vacuum gauge.

As the experimental setup is currently above Control Room 1 (CR-1) at HPEPL, it is still subject to various vibrations from the other experiments in the building to the mechanical vacuum pumps. Thus, this whole setup is placed on top of a small 3 ft. x 4 ft. optical table (Thorlabs) that is passively vibration isolated. The optical table also provides

16

many pre-drilled mounting points (1/4-20) for additional equipment such as a camera and other optics. This apparatus was evacuated using a roughing pump (Adixen 2021SD). The vacuum pressure was monitored using a Pirani Gauge. The argon working gas is provided through a Swagelok feedthrough that is connected to a bottle next to the table. The regulation of the gas input was performed manually using a manual bellows valve from Swagelok.
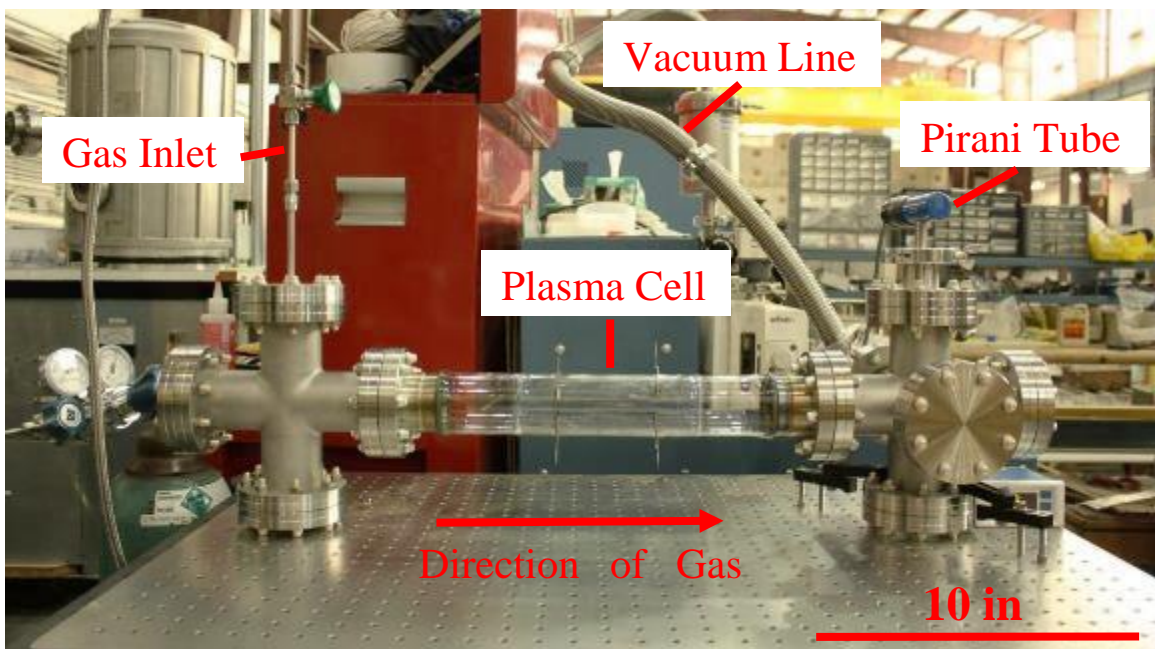
FIGURE 5 – Image of the plasma cell setup in the initial form.

The glass plasma cell was made of a 2.5-in. OD Pyrex tube with tungsten electrical feedthroughs penetrating through the glass. Tungsten feedthroughs are used due to thermal low thermal expansion coefficient and compatibility with glass. To the left and right of the glass tube, on both sides, are glass-to-metal 4.5-in. CF flanges. Figure 6 shows the plasma cell operating at 600 mTorr with 400 V DC applied between the electrodes.
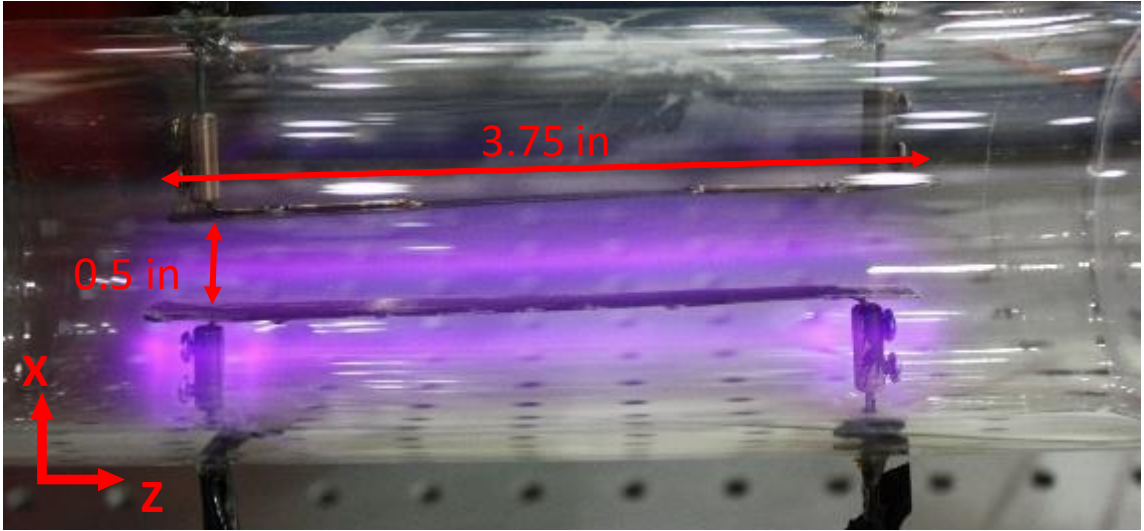
FIGURE 6 –DC plasma discharge with argon at 600 mTorr and 400 V applied voltage in our initial setup.

By building this initial plasma cell, we discovered many difficulties with tolerances from the glassblowing process and leaks due to stresses applied to the glass. It was also difficult to install, accurately set the separation distance, and modify the electrodes.

2.1.2 Evolution to Plasma Conductivity Setup

To measure the plasma conductivity, a modified setup was created. The direct tungsten feedthrough design was abandoned in favor of an electrode assembly that has wires run to the side and through a commercially-available feedthrough from Kurt J Lesker Co. One of the concerns with the electrode assembly was the distance from signal electrodes to the discharge electrode would be much shorter than between the signal electrodes. This could give a falsely higher conductivity if the signal goes through the discharge electrodes. To get an accurate measurement, the VAIPER group design incorporated a smaller discharge electrode and made the spacing of the signal electrodes much closer. Figure 7 depicts a cross-section of this shortened electrode design. The signal

electrodes are seen coming from the sides insulated by alumina tubes with only the stainless-steel ball part exposed to the plasma. The bolts attached to the green G-10 parts will serve as the discharge electrodes. The major risk with this setup is arcing between the various conductive parts. This issue initiated a redesign of the experiment and design of the electrodes.
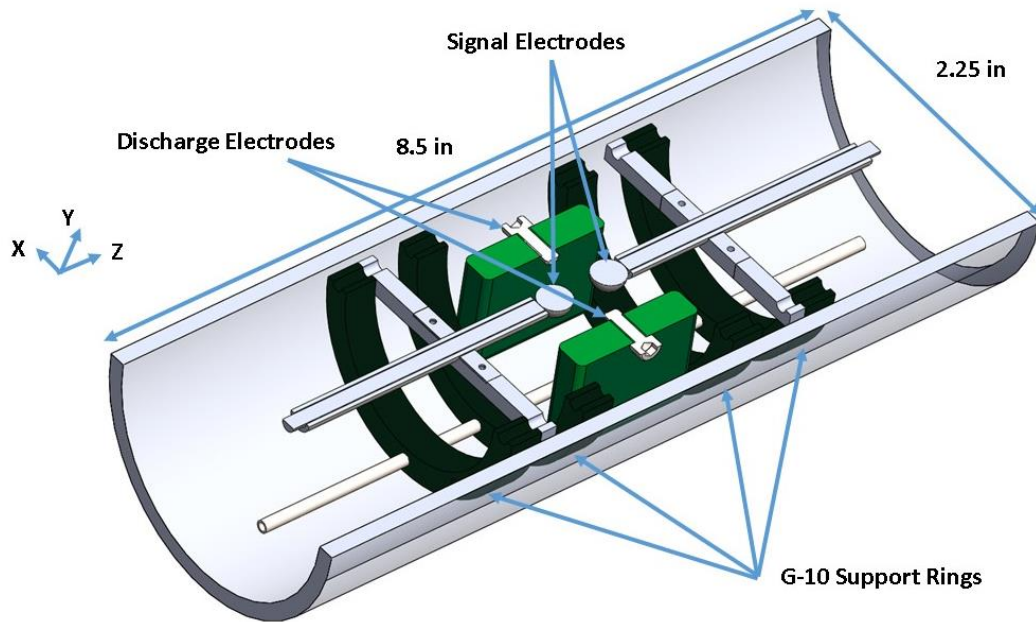
FIGURE 7 – Diagram of the small discharge electrode setup for conductivity measurements.

2.1.3 Lessons Learned

In the initial DC electrode set and the evolution, intermittent arcing between electrodes and arcing between electrodes and probes occurred often. Another problem was enhanced discharge at the screw attachment points for the assembly. These sharp points are located on the sides where the electrode and insulating G-10 structure (green rings)

19

meet and where the wires are attached to the electrodes. At the typical power level of our supplies, the G-10 insulating structures would slowly degrade with use (turn black).

In addition, the interference from the pulser to our measurement electronics made extracting the signal very difficult. This prompted the group to abandon any direct electrical plasma probing in favor of a more indirect optical method. A redesign of the electrode assembly and optical diagnostics detailed in the next section was installed.

2.2 Final Experimental Setup

The final setup for this master's thesis incorporates many changes from the lessons learned in the original setups. The main vacuum hardware changes are the glass tube, the electrode assembly and the plasma diagnostics. The final configuration is detailed in the following sections.

2.2.1 Vacuum Setup

Most of the final plasma cell remained CF parts. This design choice was made to allow compatibility with other systems in HPEPL. The only major flange change from the initial setup is the glass tube section. The flanges that attach to the glass tube section was now changed to ISO-63K. This type of flange uses an elastomeric O-ring to seal the joint and two clamps to hold the flanges together. This combination greatly reduced the stress applied to the glass to metal seals. It also reduced the time needed to remove the glass tube when it was necessary to clean or modify the electrode set. The size of the flange was an optimization between the price of parts and size of the diameter tube. This flange was the largest O-ring type flange available before price of parts doubled. An electrode set would

now be inserted or removed from the side. Any modification to the electrode assembly did

not require modification to the glass tube itself.

FIGURE 8 – Picture of the ISO-63K glass tube design employed in the final plasma experiment.

The next change from the initial setup is the mass flow control board detailed in the next

subsection. This improvement allowed us to set gas flow in a more repeatable manner.

Finally, in the last subsection, we will more fully explore our pressure regulation and

measurement scheme.

2.2.1.1 Gas and Flow Management

In this experiment, we use ultra-high purity grade argon (99.999% purity) as the

working gas of our plasma discharge. This gas is supplied by Airgas. The low cost and

abundance of argon makes it a popular gas in many plasma applications. This popularity

also makes it a well-characterized gas. The argon gas from the bottle is first regulated to

10 – 20 psig range using an Airgas Y11-215D bottle pressure regulator. The Y11-215D

model is a single stage pressure regulator with a maximum outlet pressure of 100 psig. The gas mass flow is then controlled by a 20 sccm (N_2 calibrated) MKS 1179A mass flow regulator unit on the mass flow board. The mass flow regulator unit is controlled by a MKS 247D controller. In this experiment, we typically pump the entire vacuum chamber down to approximately 1-5 mTorr and then flow argon gas to purge any outgassed trace gases for several minutes before we begin the experiment. The typical base pressure of this chamber is approximately 1 mTorr. We assume any species that are outgassed from the walls or electrode assembly remain at very low levels such that the plasma we investigate is effectively a pure argon discharge.
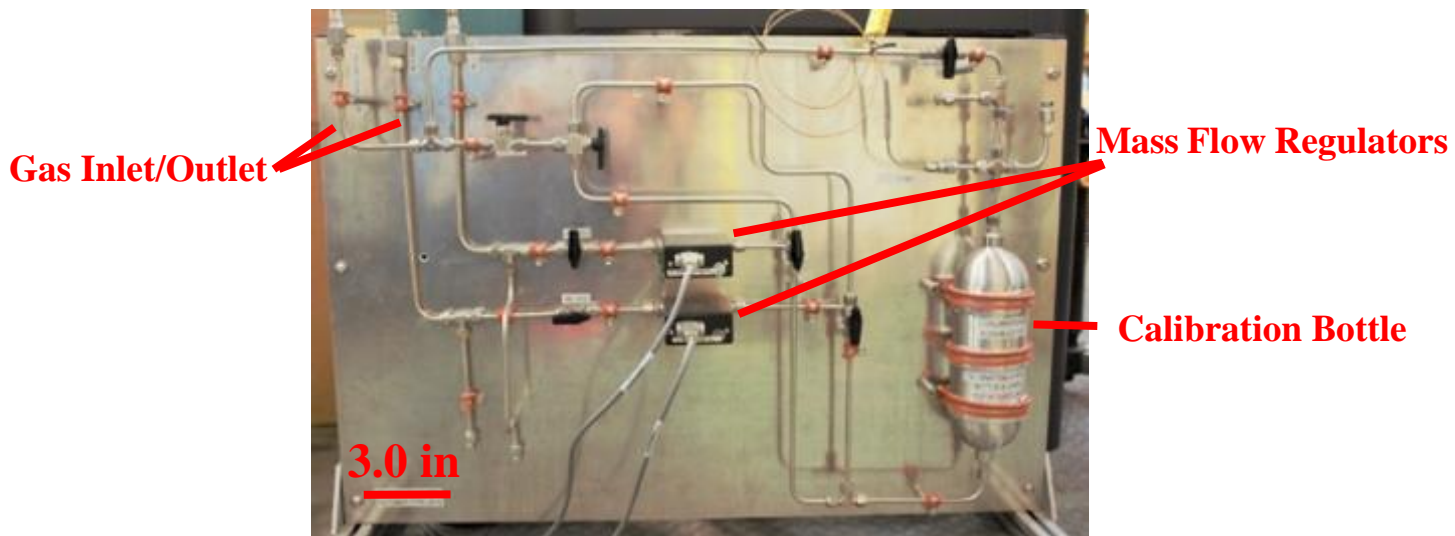
FIGURE 9 – Picture of the improved mass flow systems. This setup allowed for much more repeatable flow setting during the experimental run.

2.2.1.2 Pressure Regulation and Measurement

The Pirani gauge was invented in 1906 by Marcello Pirani [33]. The gauge consists of a heated metal wire inside the vacuum chamber and circuitry outside that measure the change in resistance due to the gas inside the chamber conducting the heat away from the

wire. As the pressure inside is lowered, the heat transfer with the wire will decrease and the wire should become warmer. The resistance of the wire is typically compared to calibrated resistors in a circuit outside the vacuum in a Wheatstone configuration.

In our experiment, we use a Kurt J Lesker 275 Series convection-enhanced Pirani gauge (KJLC 275) to measure the pressure of the working gas [34]. The measurement range for this gauge is 1 x 10^{-4} to 1000 Torr. The typical operating temperature of this gauge is between 0 °C and 50 °C. This gauge is located at the top of the 6-way cross downstream of the plasma cell. This prevents a line of sight to the plasma cell in case sputtered materials make it further downstream towards the sensor. The typical accuracy and repeatability of the gauge in the pressure range of our experiment is 10% of reading and 2% of reading respectively [34].

In the pressure ranges we test (< 10 Torr), the primary thermal paths are gas thermal conduction and radiation. The change in resistance with pressure is exploited to generate a signal. Above 10 Torr, convection currents start to circulate within the gauge and becomes the dominant heat transfer mechanism at higher pressures. Convection-enhanced gauges are specially designed to be well quantified above 10 Torr to typically 1000 Torr. The tube axis orientation is specified so that the convection works as designed for the higher pressure ranges (typically above 100 Torr).
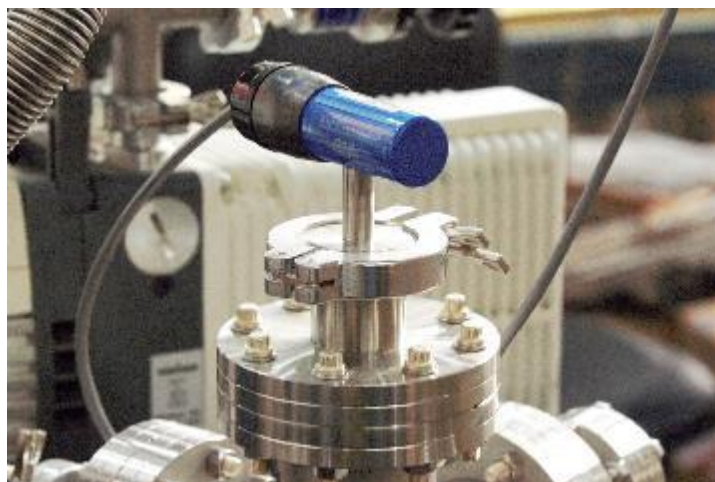
FIGURE 10 – Picture of the convection-enhanced Pirani gauge that is attached to our experiment.

A pressure calibration of this gauge is performed at atmosphere (assumed 760 Torr). If the vacuum achieves below 10^{-4} Torr, an additional zero calibration is performed. The zero calibration should be performed for accurate reading below 10^{-3} Torr. As heat conduction is gas species dependent, all readings from the KJLC 275 are pressures calibrated to diatomic nitrogen (N_2). The correction factors we use to change pressures corrected to N_2 to Ar is provided by the gauge user manual [34].

FIGURE 11 – Picture of the nitrogen (N_2) corrected pressure is readout. The conversion is made to argon using the tables contained in the manual for this gauge.

The limitations of the KJLC 275 sensor include sensitivity to contamination of the wire inside the vacuum. This can lead to erratic readings and the sensor must be sent back for cleaning. Possible sources of contamination include condensed water, hydrocarbons from the pump, or formation of coatings due to sputtering/chemistry inside the vacuum chamber. Screens may also be installed to prevent solid particles from entering the gauge.

To control our plasma cell to the desired pressure, we set the mass flow controller to maximum flow and then restrict a pumping by closing a manual bellows sealed valve connecting the roughing pump and the plasma cell. One note of caution when operating such a setup is the bellow valve is not really designed to be gating. The position of the valve can move slightly due to the vibration of the vacuum pump. In our experiment, we apply a Velcro strap to further restrict vibration-induced movement.

FIGURE 12 – Diagram depicts the regulating valve on the vacuum pump used in conjunction with the mass flow meter to control the pressure of the plasma cell.

2.2.2 Electrical Setup

The challenge in this experiment comes from both the high speeds (GHz modulation) and the high voltages (1 kV) required. Voltage and power specifications for such parts are often difficult to find or interpret. The design of the electrical aspect of our experiment comes from a mixture of intuition and experience with lower voltage dischargers, time spent on the phone with the manufacturer, and simply trial and error.

2.2.2.1   Electrical Overview

The electrical setup is split into two main parts: the measurement equipment and the pulser. Since the pulser produces broadband noise in the ground and all unshielded surrounding circuits, special care required in the grounding configuration of the electrical setup to reduce the common mode noise. Additionally, the sensitive measurement devices are placed into a shielded metal box to further reduce the noise. In addition, light from the experiment is coupled into the shielded box with fiber optics to decouple further the sensitive electro-optics.

FIGURE 13 – Picture of the shielding box that houses the oscilloscope, fast photodiode, and the spectrometer.

The line lengths that carry the high voltage pulses and their ground return are kept as short as possible. The grounds connected a common point on the stainless steel optical table. The voltage probes are kept at the lower end of the voltage divider to limit the voltage-to-ground voltage to below the rated limits. Figure 14 depicts the basic electrical setup of the experiment.
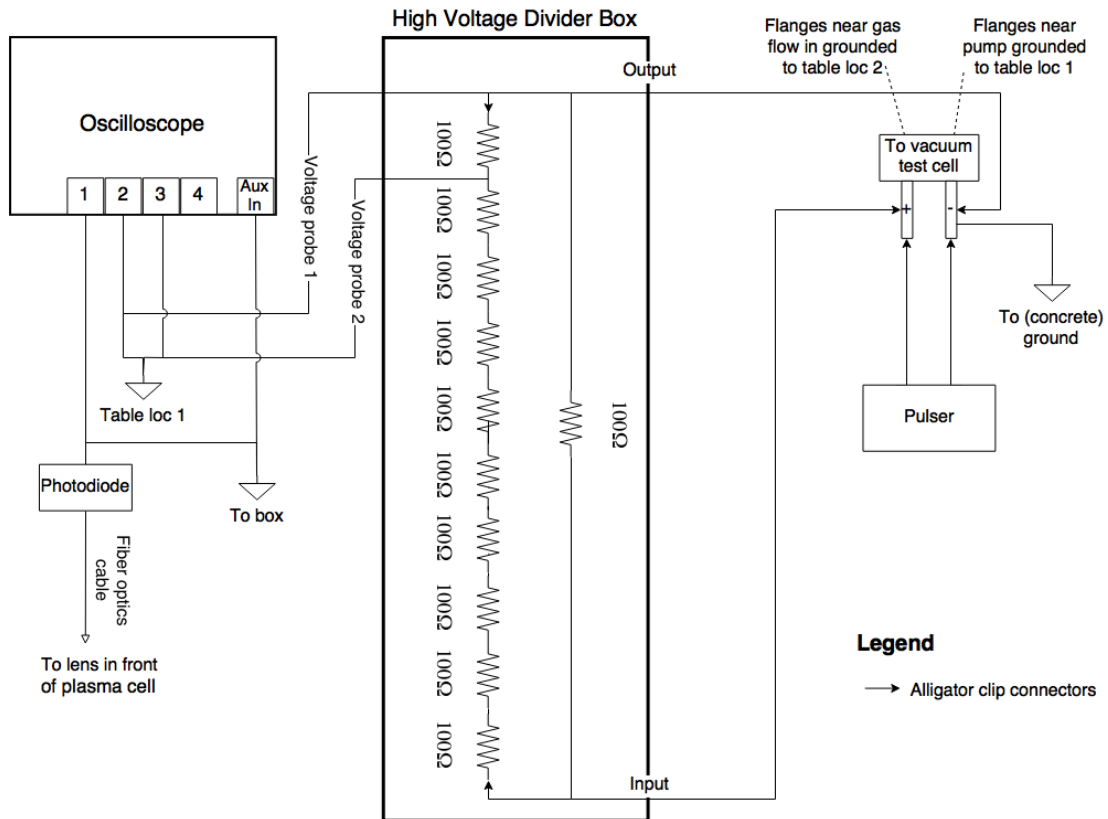
FIGURE 14 – Simplified electrical schematic of the experiment.

2.2.2.2   Discharge Electrodes

Building upon the lessons from the initial study, the electrode set was further refined to prevent arcing. Figure 14 shows this new electrode set.
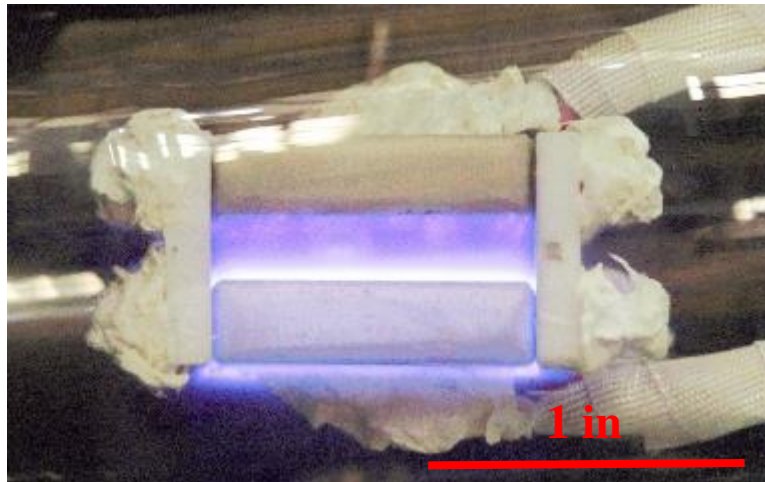
FIGURE 15 – Picture of the electrodes used in the measurements. The pulser settings are 1 kV, 50 ns pulse duration and 5 kHz repetition rate. The pressure is approximately 2 Torr argon.

The anodized electrode assembly consists of two aluminum (Al-6061) electrodes machined at the Georgia Tech Mechanical Engineering Machine Shop and anodized by Southern Aluminum Finishing Co. The electrodes are supported by white ceramic Macor spacers. A pair of Mitutoyo calipers measured the electrode spacing to be $0.20 \pm .01$ in. The area of the electrode is $1.50 \pm .01$ in by $1.00 \pm .01$ in. The thickness of the electrode is $0.25 \pm .01$ in. The anodized layer is aluminum oxide and is specified to be 0.7 mils thick. Since anodic coating have dielectric strengths of $900 - 1000$ V per mil, this layer should be able to withstand out typical discharge conditions of approximately 1000 V. This layer covers the electrode except at the threaded screw holes. This insulating layer will help reduce arcing compared to the previous electrode assembly. To prevent arcing at screw points and electrical connections, an insulating layer of high-temperature ceramic paste (Thermeez 7020) was applied. The paste appears in Figure 15 on the sides of the electrode assembly and at the connection point where the high voltgage wire connects to the electrode.

At the highest voltage setting (1 kV) and relatively high repetition rate (approx. >20 kHz) of the pulser, we do observe localized enhanced discharges on the surface of the electrode set. These regions are most likely due to imperfections of the anodization. For future electrode sets based on capacitive discharge, it is recommended to get a much thicker layer of aluminum oxide. This should encourage a more homogeneous plasma.
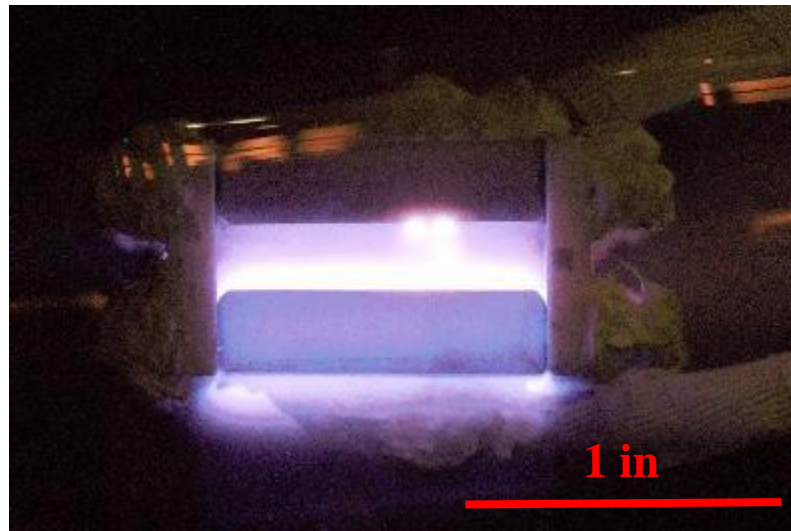
FIGURE 16 – Diagram depicts regions of enhanced discharge near the front of the electrode set (2 bright balls).

At the 3 Torr argon test points, we could not strike a glow discharge at (1 kV) without significant arcing. In future test, it is recommended to better insulate the screws or alter the design not to use screws to attach the electrode set to their supporting structures. It is also recommended to increase the anodization layer to two mils thicker than the required thickness to account for manufacturing defects.
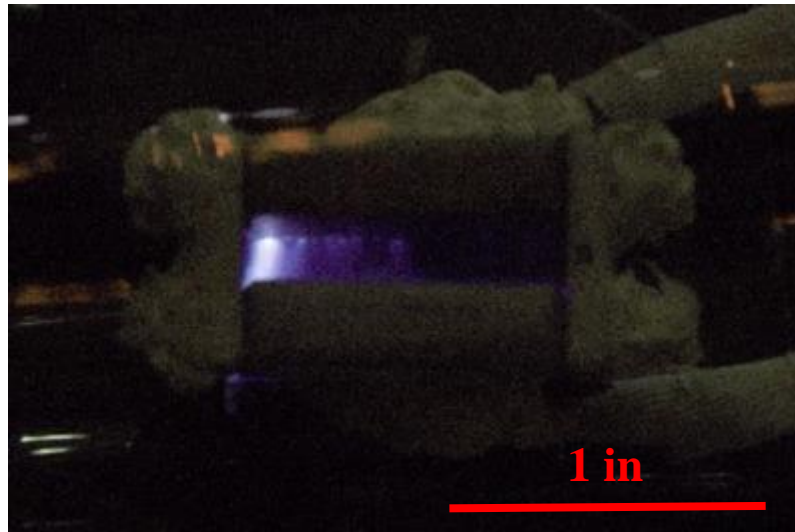
FIGURE 17 – Diagram depicts the arcing between the screw point attachments of the electrode sets.

2.2.2.3   High Voltage Pulser

For the fast-pulsed plasma power supply, we use the FPG 1-50NM100A high-voltage pulse generator [35]. The custom pulse generator is manufactured by FID GmbH. The maximum specified voltage output is 1 kV into 75-Ω load. This amplitude is adjustable from 500 V to 1000 V. The pulse has a fixed rise time of 1.2 to 1.5 ns. The pulse duration at 50% of amplitude is 5 to 100 ns. The maximum repetition rate for these pulses are 50 kHz. These pulses can be triggered using a 5-V external trigger. The pulse generator is designed to continue to operate with loads that differ from 75 Ω. It can operate in a sort open circuit mode for 20-30 seconds, but this is not considered normal operation. This pulse generator can create electromagnetic interference that can affect surrounding equipment during operation.

In this experiment, the voltage is maintained at 1 kV while as the pulse repetition rate is varied between 1 to 50 kHz and the pulse duration is set at 50 ns.

FIGURE 18 – The picture shows the FPG 1-50NM100A pulser. This pulser is located in an equipment rack next to the optical table.
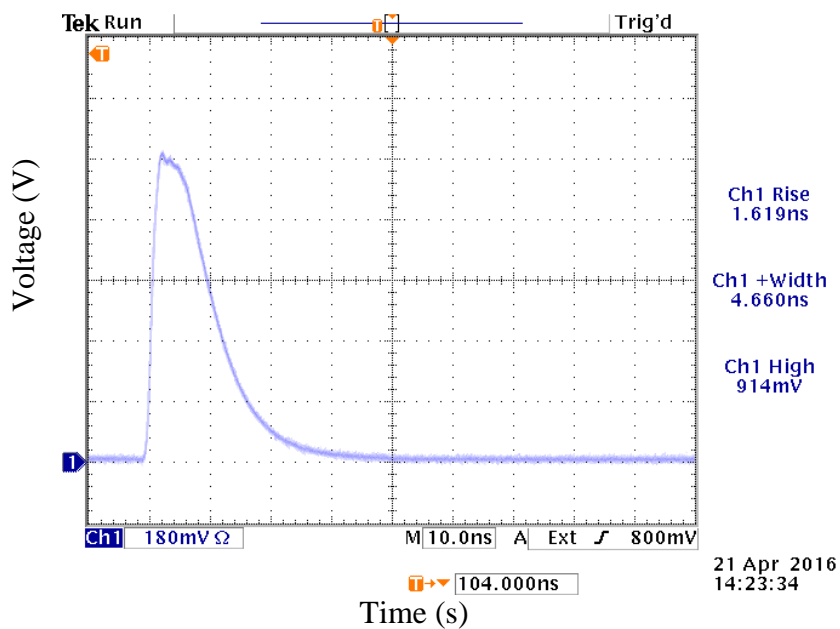
Figure 19 – The image taken from the pulser manual that shows the typical output of the pulser supply to a matched load (75 Ohm) at maximum amplitude of 1 kV and 10-ns pulse width [35].

2.2.2.4   Oscilloscope

A Tektronix DPO5104B oscilloscope is used in this experiment. The choice in oscilloscope was driven by need to use the TPP1000 probe. This model is the most updated

oscilloscope compatible with the probe. The oscilloscope bandwidth of 1 GHz also matched the probe bandwidth.

The data from the oscilloscope is recorded and transferred to a computer using a LabVIEW program. This program automatically records and saves 20 waveforms. The data is 2000 samples long and the time between samples is 0.2 ns. The acquisition of the waveform is triggered by the rising edge of Channel 2 (the first probe in the voltage divider circuit). Channel 2 and 3 measure the voltage across one resistor in the voltage divider. A custom-made MATLAB program is used to analyze the waveforms. The Channel 1 is connected by a 2-ft. long, 50-Ohm BNC cable to the avalanche photodetector. The Channel 4 is not in used.
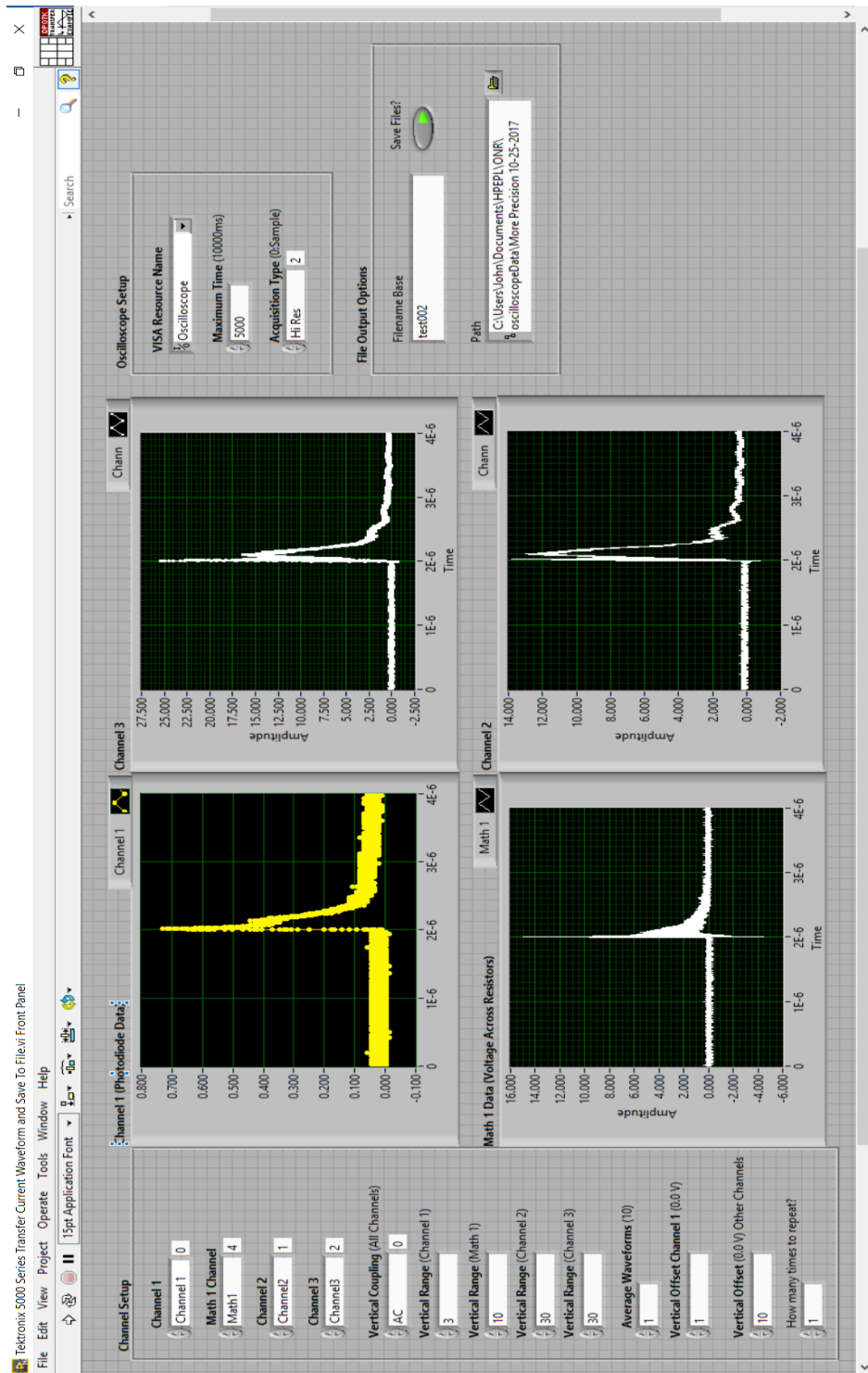
FIGURE 20 – The picture presents the LabVIEW interface that commands the oscilloscope to transfer waveforms with specified settings and save the waveforms into files on the computer for later analysis.

2.2.2.5   Voltage Divider

To monitor the pulsed, high-voltage discharge, we use a resistive voltage divider. While at first glance this may seem easy, the challenge comes due to the high voltages and fast rise times. In this regime, normal resistors are very non-ideal. Circuits designed for a certain voltage division for frequencies near DC may suffer a change of voltage division at high frequencies due to stray capacitance and inductance. These stray impedances tend to dominate at high voltages and frequencies.

To improve the measurements, several tips are suggested by the manufacturer. The suggested resistor is HVR Advanced Power Components' RT series ceramic composition resistors. These resistors are rated for high voltage and have low inductance compared to regular resistors. The total resistance of the divider should be small to reduce the RC constant of the probe/voltage divider network so that the monitoring circuit can respond as fast as the pulse (order nanoseconds). All the resistors should be the same so that the change in impedance due to stray inductance and capacitance change in the same proportion maintaining the factor of division.

It is possible to construct a voltage divider out of capacitors. This is the preferred method if the current draw due to the network divider becomes comparable to the original load under test. The suggested type of capacitor is high-voltage polypropylene film capacitors. The capacitance should be smaller than the load under test to avoid distortion due to the measurement circuit. Otherwise, the measurement circuit could act as a low pass filter. The capacitance of the divider capacitors should also be larger than the probe capacitance (typically 1 pF). This restriction is placed to prevent the measurement circuit of the oscilloscope from affecting the divider network.

34

In this experiment, we have in series 10x 100-Ohm nominal thin film resistors (TNP10SC100RFE-ND) made by Ohmite. This voltage divider is in parallel to the discharge capacitor electrodes. This resistor set is used to step down the voltage of the pulse to a safe level for the voltage probes. These resistors were originally chosen due to their high voltage specification (2000 VAC), low inductance design (high-speed circuits) and 1-W (air) power dissipation capability. The PCB board that the resistors are placed on was manufactured by Advanced Circuits. The PCB board has dimensions of 4 in. by 2 in. by 0.062 in. and is made from FR4 material.
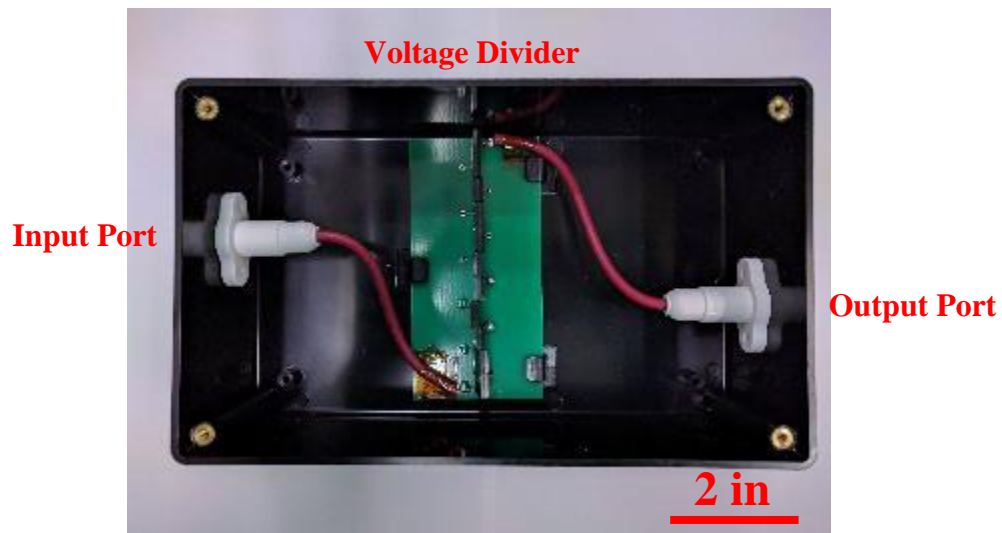
FIGURE 21 – The picture shows the recent design of the voltage divider box with the input and outputs on either side and the circuit board holding the resistors in the middle.

To get a closer impedance match to reduce reflections of the pulse, we put another large 100-Ω, 50-W Vitreous Enamel Power 270 Series Ohmite resistor in parallel to the discharge and the voltage divider. If the impedance is not close at the output of the pulser, the waveform will look distorted in the form of ringing and reflections. The amplitude of these distortions can be up to 30% of the pulse height. While the large Ohmite resistor has

more inductance than desired, the power dissipated in some smaller packaged resistors such as thin film or otherwise will increase the resistor temperature by more than 100 °C. The thin-film resistors we use are somewhat fragile and will break easily when overheated. The 50-W Ohmite resistor increased in temperature only be about 10 °C. In the next revision of the voltage divider circuit, it is recommended to use the Vishay MRA12-100-ND resistors for the voltage divider. The ceramic package makes this resistor more rugged. A suitable lower inductance power resistor like the 270 Series Ohmite has not been identified.

Additional work will need to be performed to further reduce reflections due to mixture of transmission lines we have before the pulse reaches the plasma electrodes. One possible solution is to make as much of the circuit impedances match the 75-Ω N-type connector of the pulser. This would require changing the voltage divider design and the vacuum feedthrough to match the impedance of the 75-Ω output. A low voltage pulser can be used in place of the high voltage pulser to investigate the effects of substitution safely. Any changed parts should also be verified to have the proper voltage ratings for operation.

2.2.2.6   Voltage Probes

In this experiment, we use two Tektronix TPP1000 voltage probes to monitor the voltage across a resistor in the voltage divider circuit. While the lab typically uses a Teledyne LeCroy Oscilloscopes and probes for monitoring electrical waveforms of Hall thrusters, Teledyne LeCroy does not offer voltage probes with the bandwidth required (1 GHz) to monitor the pulse with reasonably high-voltage specifications (at least 300 V). The TPP1000 is a passive 10X probe with a bandwidth of 1 GHz and 300 V. It is designed to be used with the MDO3000, MDO4000, and MSO/DPO5000 series oscilloscopes. It was

the choice in available probes that drove that oscilloscope we used. This probe has a specified signal delay time of 5.67 ns. The voltage probes were compensated when connected to the oscilloscope as recommended by the user manual. One probe clipped into the common of the pulser and the other probe clipped to the last resistor.

FIGURE 22 – Picture of one of the two TPP1000 probes employed to measure the voltage across the last resistor in the voltage divider circuit.

It is important to point out the probes are ground referenced. Both the oscilloscope and ground clip of the probe must be connected to ground and not allowed to float. Otherwise additional noise or damage can occur to the oscilloscope/probes. Unlike a differential probe that has two leads that can be connected to a floating common voltage, ground-referenced probes usually increase bandwidth by reducing capacitance. This is achieved by removing the insulating material between the signal and the ground shield. It is therefore not a surprise to see an inverse relationship between bandwidth and voltage rating among the commercially available voltage probes. If higher voltages are investigated

in the future, a more careful redesign or perhaps custom voltage measurement system may

need to be fabricated.
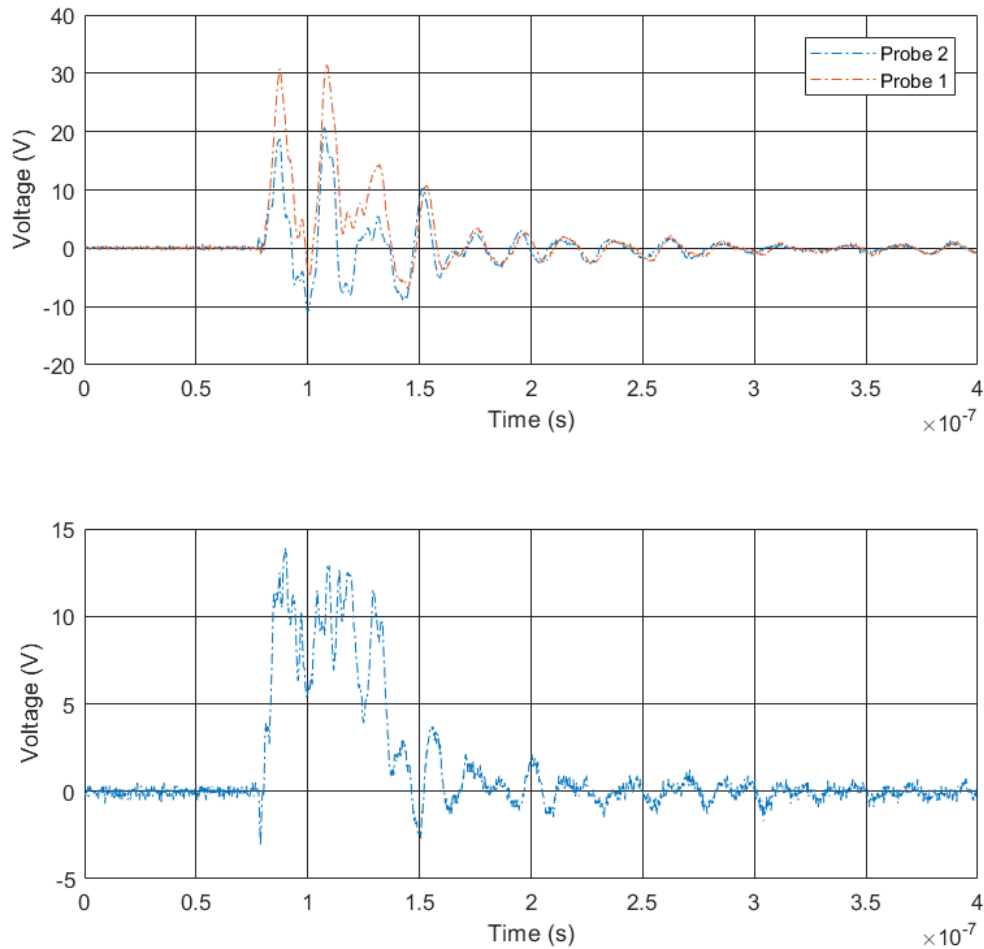
FIGURE 23 – The image presents 20 averaged 1 kV, 50-ns pulse measured using the TPP1000 probes and the DPO5104B oscilloscope. The raw waveforms (above) of each probe and the actual voltage pulse across the resistor (below). The combination of the probe (1/10) and the voltage divider (1/10) results in a 1/100 division in voltage.

2.2.3 Optical Setup

In this experiment, a spectrometer and a fast photodiode are used characterize our plasma. The spectrometer and the fast photodiode are placed inside the shielded equipment box along with the oscilloscope. The light is collected by a 2-m long Thorlabs M59L02 step-index fiber patch cable. This fiber cable has a core of low-OH, pure silica Ø1000 μm that has an index of refraction of $n = 1.44$. It has a numerical aperture of 0.50. This value means the fiber optic has approximately a 40° acceptance angle.

Plasma Cell

Fiber Optics Port

To Fiber Output

Calibration Light Source

40 °

1.4 in

Electrodes
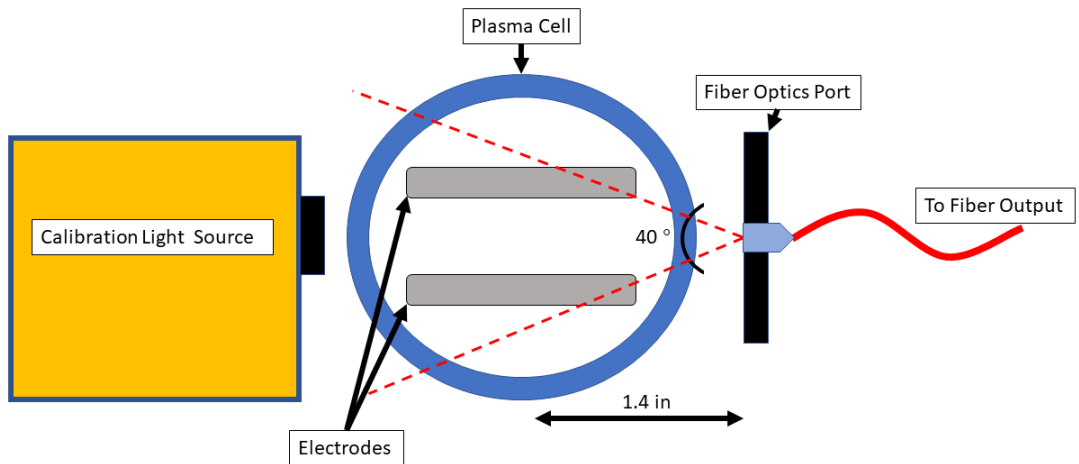
FIGURE 24 – Schematic of the sideview of the collection optics geometry with the plasma cell. It also depicts the placement of the calibration sources. The fiber output is connected to either the spectrometer or the photodiode depending on the measurement.

2.2.3.1 Spectrometer

In this experiment, the compact USB grating spectrometer is used to characterize the plasma. This section describes the methods, setup, and equipment used to calibrate the

measurements made using the HR4000CG-UV-NIR spectrometer [36]. The fiber optic collecting light from the plasma cell connects directly to the SMA connector on the spectrometer. A summary of the specifications taken from the Ocean Optics manual for this spectrometer is listed in the table below.

Table 1. Specifications for the HR4000CG-UV-NIR spectrometer

Specifications	Values

Physical Specifications
 	
    Physical Dimensions:
 	
    Weight:
	
	148.6 mm x 104.8 mm x 45.1 mm
	
	507 g

Power
 	
    Power requirement:
 	
    Supply voltage:
	
	500 mA at +5 VDC
	
	4.5 V - 5.5 V

Spectrometer
 	
    Design:
 	
    Wavelength Range:
 	
    Focal length (input):
 	
    Focal length (output):
 	
    Input Fiber Connector:
 	
    Grating:
 	
    Entrance Slit:
 	
    Detector:
 	
    Integration Time:
	
	Asymmetric Crossed Czerny-Turner
	
	200 nm – 1100 nm
	
	F/4 101 mm
	
	68 mm
	
	SMA 905
	
	HC-1, 300 lines per nm
	
	5-µm wide
	
	Toshiba TCD1304AP
	
	3.8 ms – 10 s

Dynamic Range:	2500 single integration period
Signal-to-Noise:	300:1 single acquisition
Readout Noise (single dark spectrum):	6 counts RMS, 20 counts peak to peak
Optical Resolution:	<1.0 nm FWHM
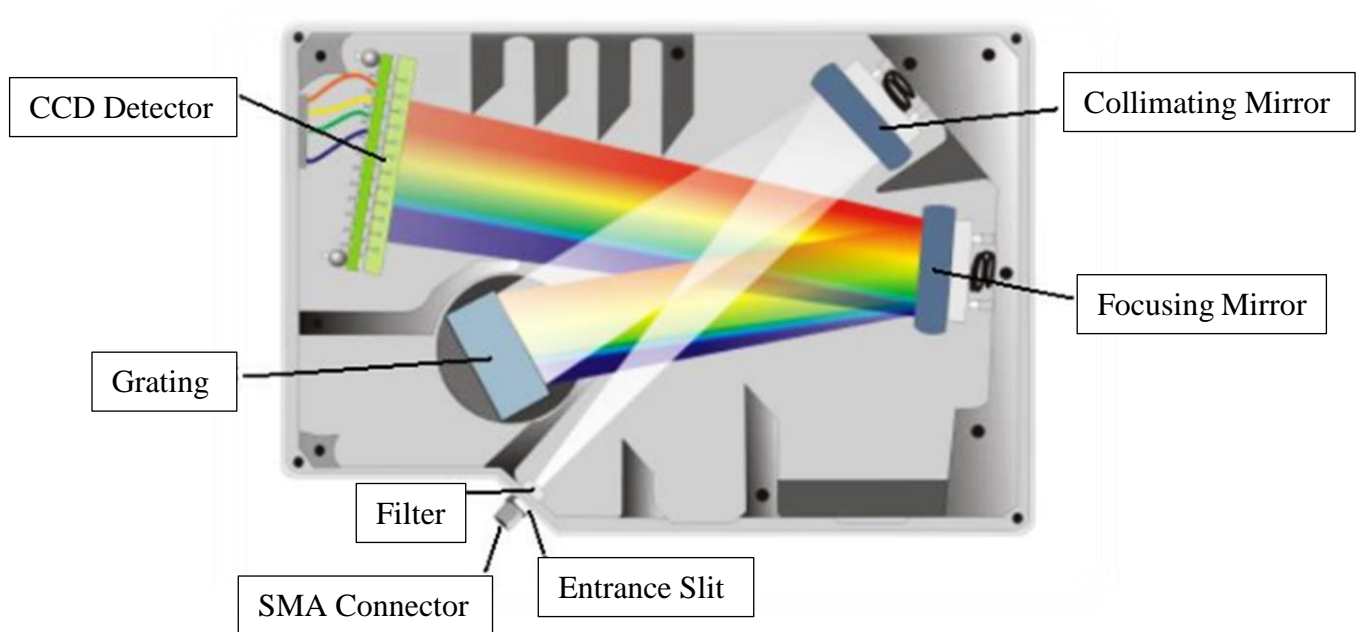
FIGURE 25 – Diagram a basic schematic of a Czerny-Turner spectrometer from Ocean Optics [36]. This diagram is taken from the Ocean Optics spectrometer manual. It details the sequence of parts the light interacts with in the spectrometer.

Wavelength calibration data must be taken once a day to ensure there has been no shift on the instrument and to accurately determine emission line positions. This setup is shown in Figure 24. The calibration will shift as a function of temperature and environmental conditions. To calibrate our spectrometer, we employ a known light source with well-characterized emission lines. In our experiment, we use the Ocean Optics Hg-1 light source [37]. This is a low cost, compact, low-pressure gas discharge based on mercury and argon. The emission lines span approximately 253 nm to 922 nm. This source requires

one minute to stabilize and has an SMA 905 fiber connector and powered by a 12 VDC power supply. This one minute is required for the emission lines from the discharge to reach steady state. The ambient temperature is recorded during the data gathering and varies less than 1.5 °C during a test run. Thus, we can discount temperature drift effects changing the calibration significantly over the data gathering run.

FIGURE 26 – Picture of the Hg-1 wavelength calibration unit used at HPEPL.

To capture the wavelength calibration data, 20 dark spectra measurements are made and averaged. 20 measurements with the Hg-1 are made and averaged to determine the average spectrum of the wavelength calibration and associated errors. The averaged dark spectrum is subtracted from the averaged Hg-1 calibration spectrum. A MATLAB algorithm then goes through and identifies the groups of pixels that represent the emission lines in this spectrum. A fit is applied to the emission lines to determine the center position. This set of positions are compared to the known positions of the lines given by the

manufacturer. A least-squares fit is employed to determine a 3rd-order polynomial fit coefficients for the wavelength correction. This polynomial correction and the sets of dark spectra are employed to correct the subsequent data gathered that day.

We use a different spectrally broadband light source to characterize the wavelength dependence of our measurement apparatus. This intensity response correction must be performed to ensure our emission calculations is due to physical processes in the plasma rather and not due to the optical properties of our measurement apparatus. The largest effect on the intensity of the ultraviolet range in our experiment is due to the transmission properties Pyrex tube that holds the plasma cell. The transmittance of Pyrex drops from about 95% at 350 nm to approximately 0% at 230 nm [37]. For further investigation of ultraviolet emission lines, it will be necessary to alter the material of the plasma cell. In the 350 nm to 1200 nm range, the greatest source of intensity response as a function of wavelength is due to the grating employed in the HR4000CG-UV-NIR spectrometer [38].

FIGURE 27 – Picture of the SL1-CAL intensity calibration light source used to calibrate the spectrometer

For this experiment, we use the SL1-CAL light source made by StellarNet, Inc. This light source is a krypton filled, tungsten halogen lamp with an effective spectral range between 350 nm and 2500 nm. The SL1-CAL simulates a 2800 K blackbody spectrum and comes with a NIST traceable, absolute intensity calibration data. This source has an output power of 200 per m^2 and a bulb life of over 10,000 hours. This source is placed on the other side of the glass tube of the plasma cell pointing directly at the fiber optic. When gathering data for this experiment, we assume the error in the measurement is shot noise limited.
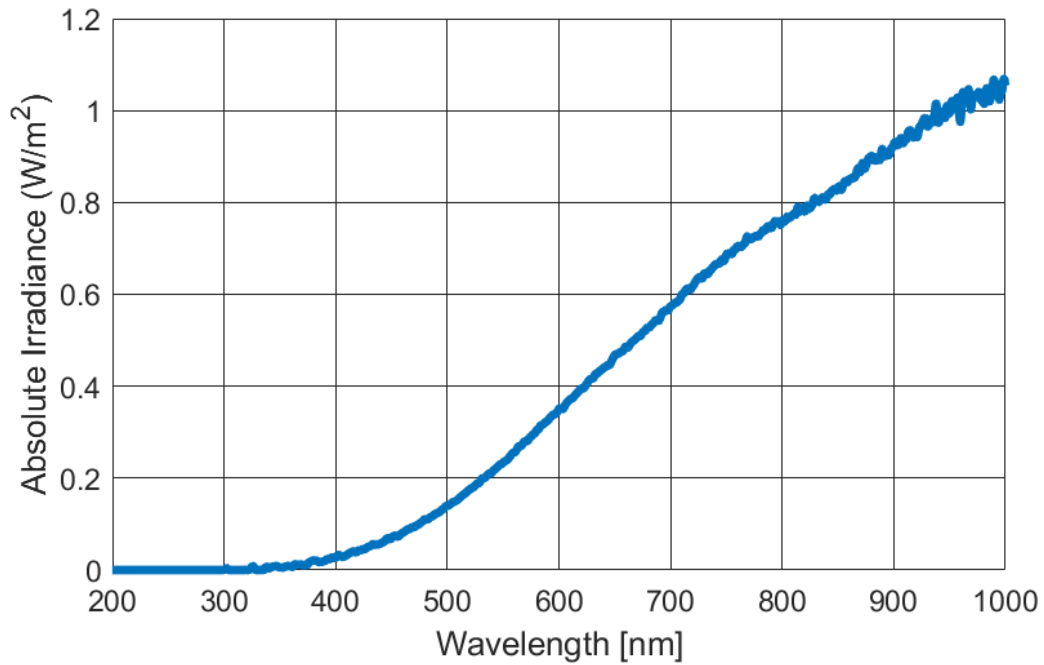
FIGURE 28 – Diagram depicts the NIST traceable calibration spectrum provided with the tungsten lamp.

2.2.3.2 Photodiode

We will use a Thorlabs APD430A2 silicon avalanche photodiode to measure the light emission from our plasma cell. The effective wavelength range of the detector is 200 nm to 1000 nm. This photodetector has an active area diameter of 0.2 mm. The output

bandwidth is DC to 400 MHz. The maximum output voltage is 4.1 V. The optical damage threshold is 1 mW. For simplicity, the fiber patch cable is directly connected to a threaded SMA adapter installed on the detector. The detector is also placed inside the shielded electronics box for pulser noise rejection purposes. The detector gain is always set to the maximum value (max output voltage 4.1-V) for the measurements taken in this experiment. It is recommended that the gain be set to min before a new application is performed. For higher sensitivity applications in the future, it is recommended to have a collimator and focusing lens assembly at the photodetector input to compensate for beam divergence out of the fiber. Care must be taken not to exceed the damage threshold however.

While amplification is important to increase signal to noise, it is also important to check the experimental setup for noise sources. Careful shielding of the high voltage pulser supply is necessary. Ferrite beads to filter common mode noise in the AC power lines. The pulse noise can be seen on the AC lines during operation. Changing which electrical outlet to plug into does alter the signal. The whole setup is plugged into a common wall outlet. The newer oscilloscope (Tektronix DPO5104B) also has better common mode noise rejection compared to the previous oscilloscope (Tektronix TDS3034B). Lastly, the grounding for both the instrumentation and power supplies should have the lowest possible impedance path to ground as possible. Otherwise, these pulse sources will transmit through the ground reference affect the measurements performed on the instrumentation.
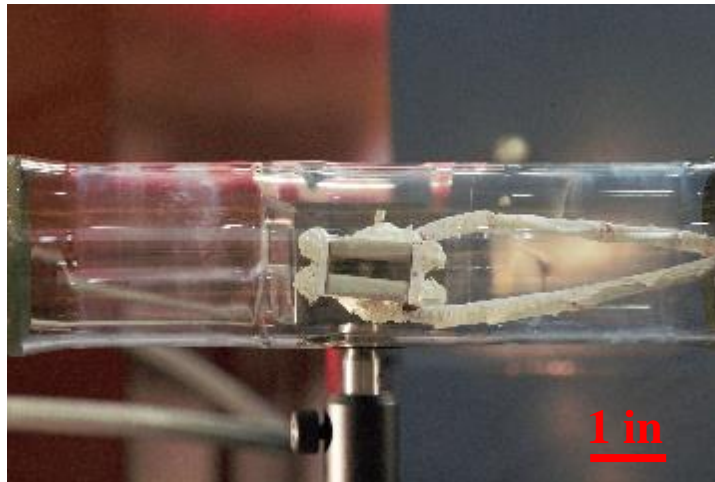
FIGURE 29 – Picture of the electrode set and the fiber light collector positioned to collect light from the middle of the discharge

2.2.3.3 PrismSPECT

In our study, we use a commercial collisional-radiative analysis code called PrismSPECT. This software performs detailed calculations of the properties of laboratory plasmas like expected emission spectra, ionization fractions and atomic level populations based on input parameters. We use the version 6.5.0 of the code created by Prism Computational Sciences, Inc.

This software incorporates the following atomic processes in collisional-radiative modeling: collisional ionization, recombination, excitation and de-excitation; photoionization and stimulated recombination; photoexcitation and stimulated emission; spontaneous decay; radiative recombination; and dielectronic recombination, autoionization, and electron capture. The emission lines produced also incorporate Doppler and Stark broadening. PrismSPECT uses the ATBASE suite of atomic codes for calculating cross-sections for various atomic processes. Atomic-level energies and oscillator strengths use NIST values when available.

Once we determine an estimate for the electron temperature and define gas conditions, the software can calculate the electron density. In this calculation, we also assume local thermodynamic equilibrium.

CHAPTER III – PLASMA RISE TIME MEASUREMENT

In the plasma rise time measurement, we use an unfiltered avalanche photodiode detailed in the previous chapter to monitor the discharge. We connected the output of the fiber optic patch cable to the avalanche photodiode. The discharge waveforms and the light curve from the photodiode are digitized on the oscilloscope and the raw data is later analyzed on a computer using MATLAB code.

3.1 Plasma Rise Time Measurement

We investigated the effect of pulse repetition rate on the plasma rise time. We fixed the pulser to a setting of 1 kV and 50-ns pulse duration. The pulser repetition rate was set to the following values: 1 kHz, 5 kHz, 10 kHz, 25 kHz, and 50 kHz. For this measurement, the pressure in the plasma cell was regulated to within 1.0 ± 0.2 Torr and 2.0 ± 0.2 Torr corrected for Argon. The pressure was allowed to settle for at least 2 minutes before measurements were made. If the pressure changed more than 0.1 Torr within that time, the regulator would be re-adjusted until the pressure stabilized at the desired point. The error in the pressure measurement was dominated by instrument accuracy. Between each measurement condition, there was a rest time of one minute where the discharge supply was turned off to clear any hysteresis effects between each condition. At the beginning of each condition, there was a 1-minute warm-up period where the discharge was enabled but no measurements were taken.

Figure 27 and Figure 28 details averaged waveforms of the pulses at the various test conditions. For each condition, we took 20 scans and averaged the waveforms. Note that the waveforms from Figure 27 and Figure 28 are not propagation delay corrected. The

ripples in the photodiode waveform is due to imperfect nature of the high-voltage pulse (reflections etc.) discharging unevenly over the pulse and electrical interference the photodiode circuit receives from the pulser. The measurement of the rise time is calculated using a smoothed light curve to avoid miscalculation associated with the unsteady discharge voltage ripples. The rise time is defined as the time for the light curve to rise from 10% to 50% of the maximum amplitude of the light curve. This definition is used to avoid the differences that occur later in the pulse due to the discharge condition affecting the pulse. For both figures, the pulse waveform voltage is 100x the value shown in the plot due to the division of the voltage divider and voltage probe.
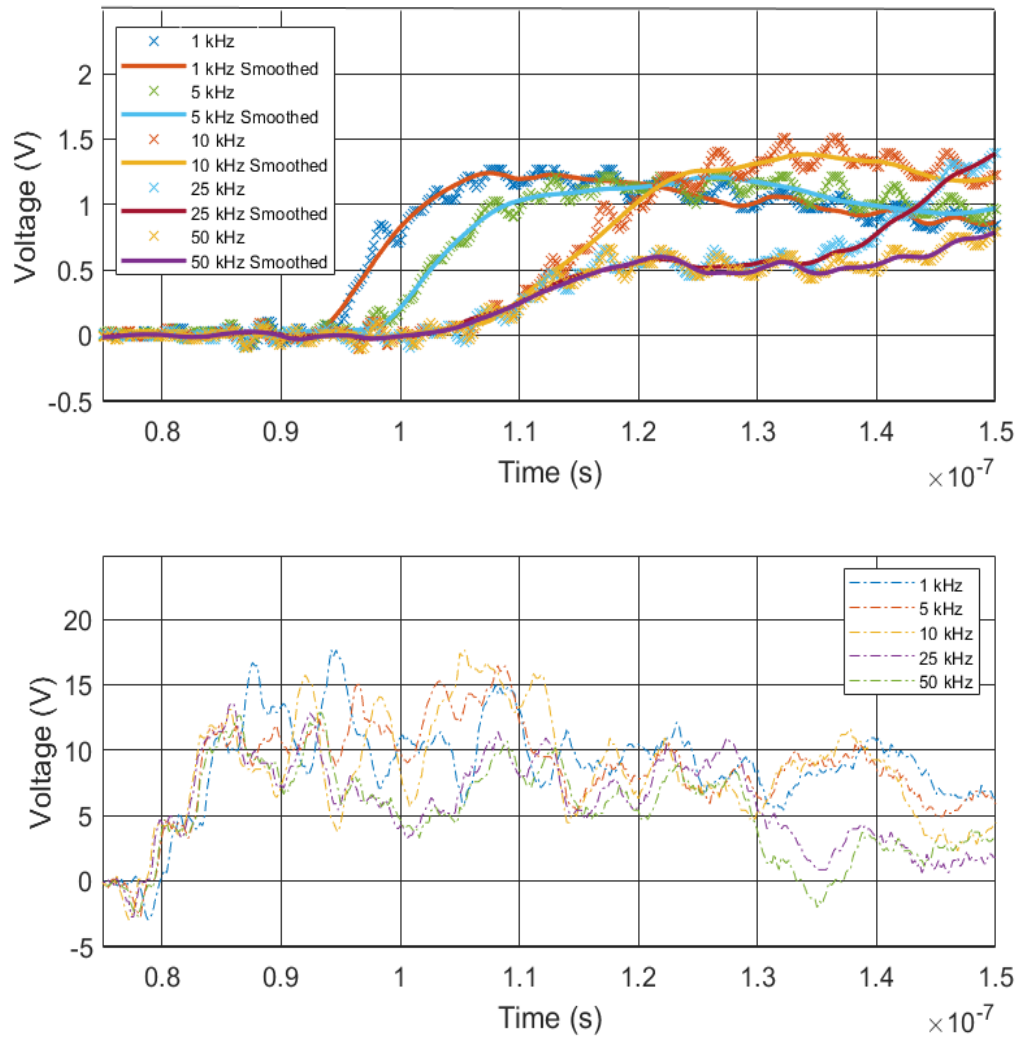
FIGURE 30 – Diagram depicts the voltage output of the photodiode (above) and pulse waveform measured at the voltage divider resistor (below) for a 1 kV and 50 ns pulse duration discharge at 1 Torr argon for various pulse repetition rates. The pulse starts at approximately 79 ns.
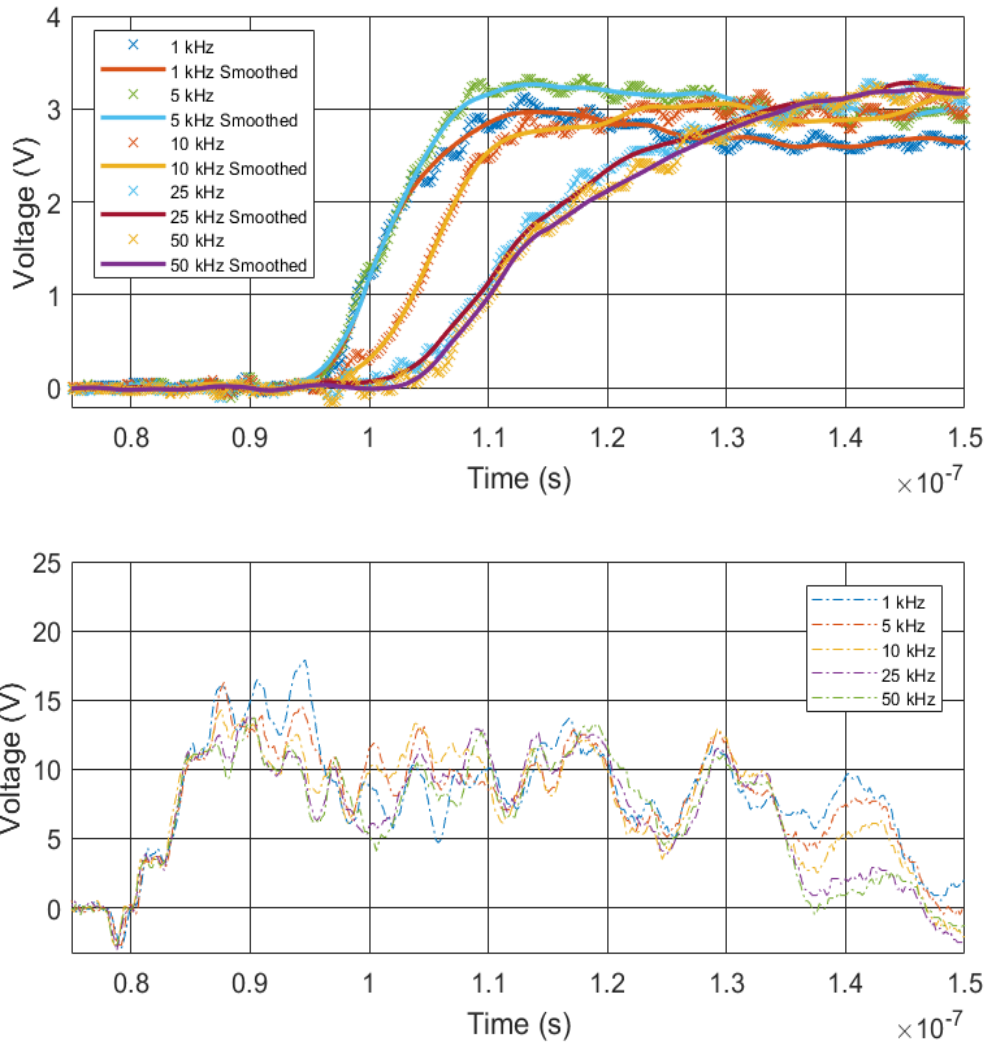
FIGURE 31 – Diagram depicts the voltage output of the photodiode (above) and pulse waveform measured at the voltage divider resistor (below) for a 1 kV and 50-ns pulse duration discharge at 2 Torr argon for various repetition rates. The discharge pulse starts at 80 ns.

51
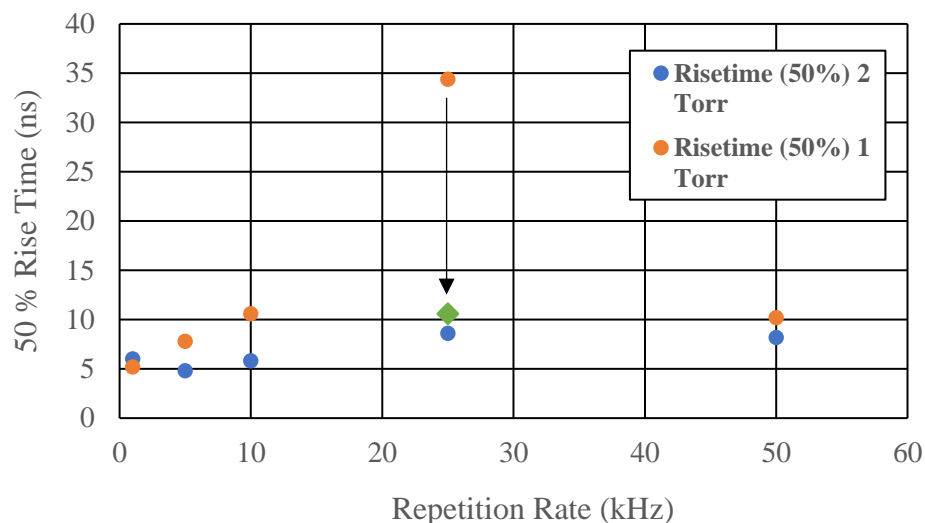
FIGURE 32 – Plot depicts the calculated rise time (10% to 50%) of the optical emission of the pulsed plasma. One data point shown as the green diamond was manually calculated after an inspection of the results of the Matlab analysis code. The arrow points from the original calculated value to the manually revised value. The uncertainty in time is estimated to be 0.5 ns.

3.2 Rise Time Discussion

In general, the rise time of the light curves are within a factor of about two of what the modelers had originally predicted for the rise time of electron density using a similar geometry and discharge condition. The next step would be for the modelers to verify the plasma evolution for these specific conditions in order to make a proper comparison. As the light curves represent an upper limit to the electron rise time, it shows (even at a modest discharge voltage of 1 kV) our goal of plasma initiation on the nanosecond timescale is achievable. In order for a rise and peak of the optical emission, the electron density must rise and peak just before the light curve rises if we assume the plasma is mainly collisionally excited during this period.

In the 1 Torr case in Figure 30, both the 25 kHz and 50 kHz conditions exhibited a drastically different light curve and discharge voltage waveform compared to the low repetition frequency cases. As the sensitivity of the photodiode is limited to the $200 - 1000$ nm range, it could be additional UV transitions are not being captured. Experimental confirmation of this would require reconstruction of the glass tube and a new set of UV compatible optics. This upgrade would be a very expensive side experiment to determine the cause of this behavior. As we do not see this behavior in the 2 Torr case, it may not be an issue for our application which will ultimately targets higher than 2 Torr pressures.
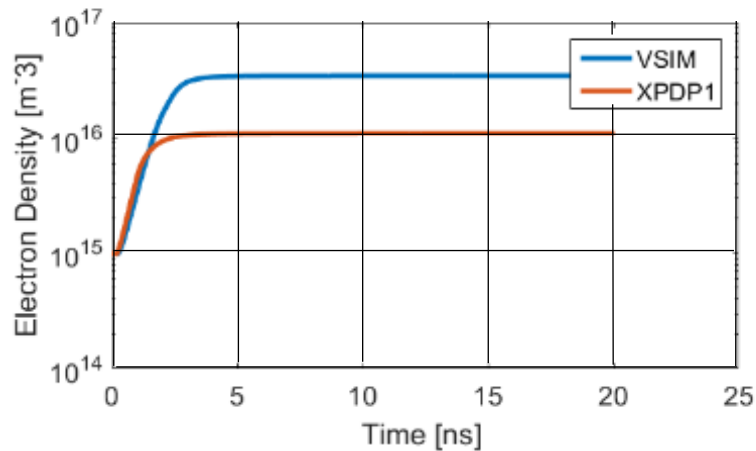
FIGURE 33 – Predicted electron density as a function of time for a 1 cm gap between electrodes and 1 kV pulse with 2-ns duration starting with 10^{15} m^3 electrons.

In both Figure 30 and Figure 31, we see a trend of longer delay time between voltage pulse initiation and the rise of optical emission. Taking into account of the different propagation times of the voltage probes vs the photodiode signal of approximately 7 ± 2 ns, we can see there is a variation of approximately 5 to 20 ns delay time between the pulse and the optical emission of the plasma. Under the optically thin plasma assumption, the light we detect is mainly from the radiative decay. From the spectroscopy results in the

next section, we see the light emissions mainly in the 700 nm to 850 nm range with radiative lifetimes of approximately 10 ns to 25 ns. One explanation for the variation is longer lifetime levels are being populated preferentially at the higher pulse repetition rates. An investigation with a series of narrowband filters at these transitions could clarify the cause of the delay.

For the plasma antenna to work, multiple sections of discharge cells must be timed to an accuracy higher than the propagation time of the VLF signal in each plasma section. Depending on the geometry of each individual electrode section, this timing should be typically better than approximately 10 picoseconds (if we assume an electrode of 1 in along the propagation direction and maximum error of 0.1 inches allowed for the wave). If the timing of the rise of the electron density is very dependent on the pulse repetition rate, this should be first investigated using modeling. A later verification can be performed by measuring how the amplitude modulated VLF pulses become distorted due to controlled timing offsets (simulated mis-timing or jitter) as it travels through one plasma cell.

Lastly, there is additional aspects of the pulser that need to be verified. The initial 10-ns to 15-ns part of the voltage waveforms have differences of less than 100-V between each of the cases. It should be verified again that the voltage waveforms do not vary with pulse repetition rate when loaded into a constant impedance source to eliminate the supply as the cause of the difference. If the waveforms do remain similar under a constant load, this would be an indicator that the discharge variability as a function of time during the duration of the pulse. To achieve even faster rise times, a sharper pulse and higher voltage will be required. Our pulser has an ideal rise time of ~1.5 ns, but our measured pulse rise time is more in the 5 – 10 ns range. An investigation into improving the discharge circuit

54

should be made. With a finite rise time pulse waveform, our modelers predictions may come into closer agreement. The modelers currently assume an ideal step function voltage pulse to calculate the plasma properties.

CHAPTER IV – PLASMA SPECTROSCOPY

In the plasma spectroscopy measurement, we connect the fiber optic patch cable to the SMA port of the HR4000CG-UV-NIR spectrometer instead of the photodiode. Similar to the last test, we fixed the pulser to a setting of 1 kV and 50 ns pulse duration. The pulser repetition rate was set to the following values: 1 kHz, 5 kHz, 10 kHz, 25 kHz, and 50 kHz. The pressure in the plasma cell was regulated to within 1.0 ± 0.2 Torr and 2.0 ± 0.2 Torr corrected for argon. The pressure was allowed to settle for at least 2 minutes before measurements were made. The error in the pressure measurement was dominated by instrument accuracy. Between each measurement condition, there was a rest time of 1 minute where the discharge supply was turned off to clear any hysteresis effects between each condition. At the beginning of each condition, there was a 1-minute warm-up period where the discharge was enabled but no measurements were taken.

4.1 Spectroscopy

To correct for electronic noise, 20 dark spectra were collected at the beginning of each data run. For each condition (including the dark condition), we collect 20 spectra and take the numerical mean. The averaged spectra for each condition is then corrected for dark noise, wavelength calibration and intensity calibration (detailed in the Chapter II) using a custom set of Matlab code created at HPEPL. Since optics and electronic noise is sensitive to temperature changes, we monitored the temperature during the test run. A temperature change of no more than 1.5 °C was registered.

Once the corrected, averaged spectra for each condition are produced, we use another custom MATLAB code to find and identify emission lines with Ar I and Ar II emission lines from the NIST Atomic Spectra Database. After the identification of the emission lines, I use the other atomic information provided by the NIST database to complete our analysis. To create a Boltzmann plot, I combine the relative intensity calibrated data with the information in the following table obtained from the NIST Atomic Spectra Database [32]. These lines are found in each condition so the comparison between each discharge condition is more consistent. I use PrismSPECT (detailed in the previous section) to generate an estimate of the electron density based on pressure and electron temperature with the assumption of LTE.

Table 2. Wavelengths and atomic data used in calculations (for the 2 Torr case we use a subset of these lines since not all were detected consistently across the repetition conditions) [32].

Wavelengths (nm) Vacuum	$g_k A_{ki}$ (s^{-1})	Energy of Upper Level (eV)
714.901	1.88×10^6	13.28264
727.494	5.49×10^6	13.32786
738.601	4.24×10^7	13.30223
750.594	4.45×10^7	13.47989
751.672	4.02×10^7	13.27304
763.721	1.22×10^8	13.17178
772.589	3.51×10^7	13.15314
801.699	4.64×10^7	13.09487
811.754	2.32×10^8	13.07572
810.592	7.50×10^7	13.15314
826.679	4.59×10^7	13.32786
841.052	1.12×10^8	13.09487
842.696	1.08×10^8	13.30223
852.378	4.17×10^7	13.28264
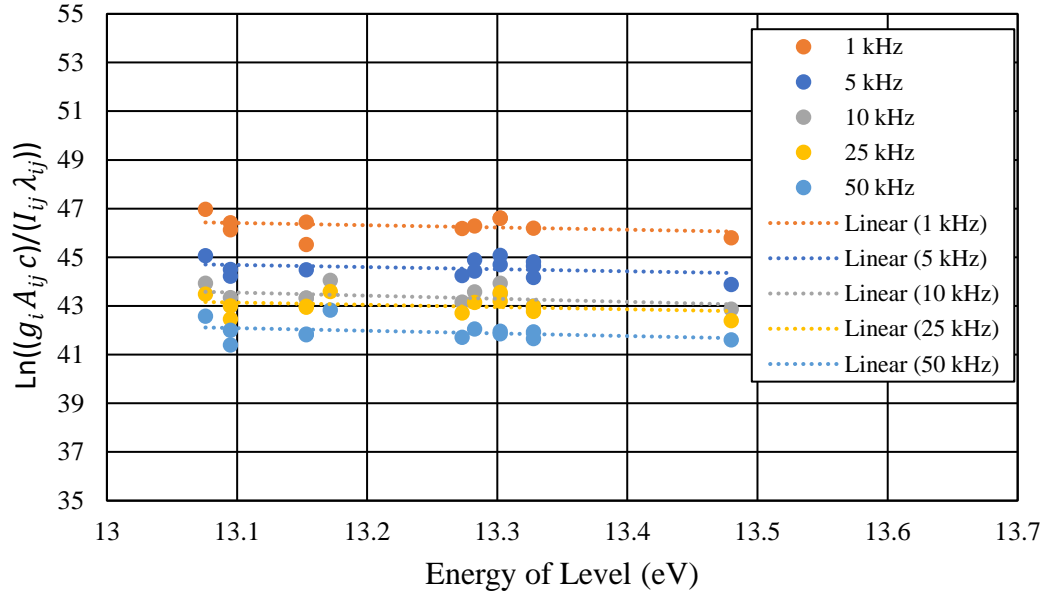
FIGURE 34 – Boltzmann plot calculated from the 1-Torr argon data with various pulse repetition rates.
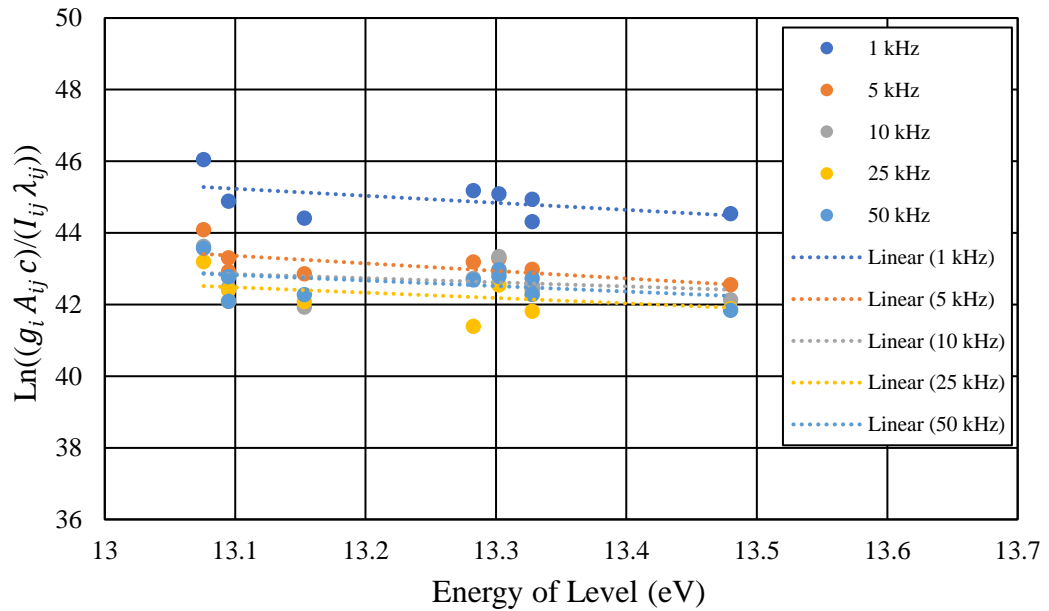
FIGURE 35 – Boltzmann plot calculated from the 2-Torr argon data with various pulse repetition rates.
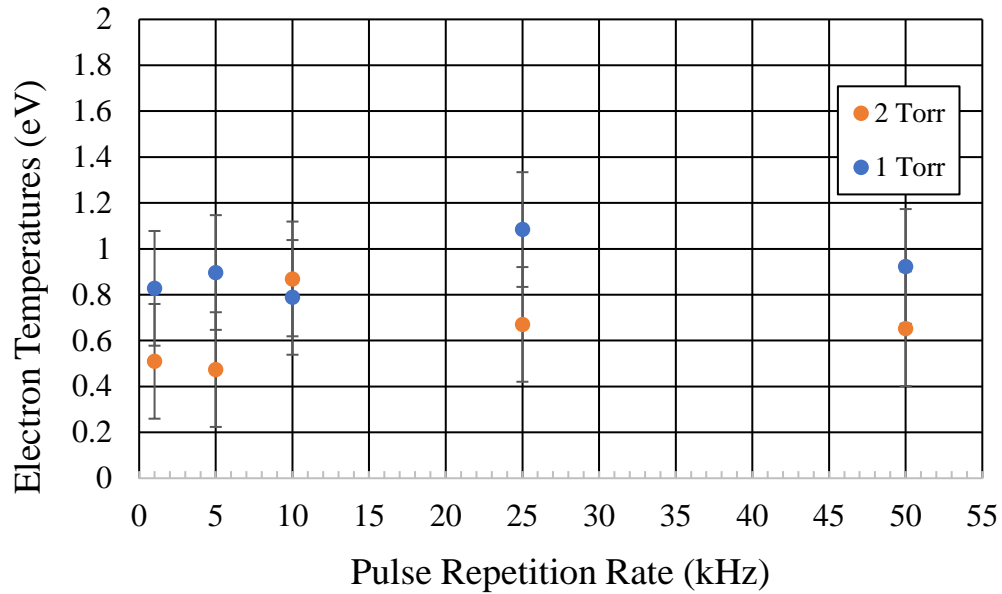
FIGURE 36 – Diagram depicts the calculated electron temperatures and an estimate of the errors.

4.2 Spectroscopy Results Discussion

For a given discharge voltage, pulse repetition rate and pulse duration, I do expect the electron temperature of the 2-Torr case to be lower than the 1-Torr pressure case. This is due to the increase in inelastic collisions the electrons in the 2-Torr case will encounter due to a smaller mean free path. Qualitatively, the pressure dependence behavior of the electron temperature is reasonable.

FIGURE 37 – Diagram depicts the calculated electron number density using the calculated electron temperatures and PrismSPECT with LTE and Non-LTE assumptions for argon.

Using PrismSPECT and the calculated electron temperatures, I can generate an estimate of the electron number densities presented in Figure 38. These electron number densities estimates result in a plasma frequency of approximately 1 THz for the 1-Torr case and 50 GHz to 1 THz in the 2-Torr case if we assume LTE plasma. Choosing the non-LTE plasma results in lower plasma density estimates. The difference is approximately 1 to 2 orders of magnitude for the 1-Torr case and approximately 2 to 5 orders of magnitude for the 2-Torr case. Figure 39 illustrates the difference in calculated electron density as a function of electron temperatures. This illustrates the sensitivity of the electron density to model assumptions in the input for the PrismSPECT model. In the non-LTE case, there are additional options to modify the effect of atomic processes. We use the default case for the

non-LTE calculations, but the fine tuning of these processes may lead to results more in line to experimental findings.
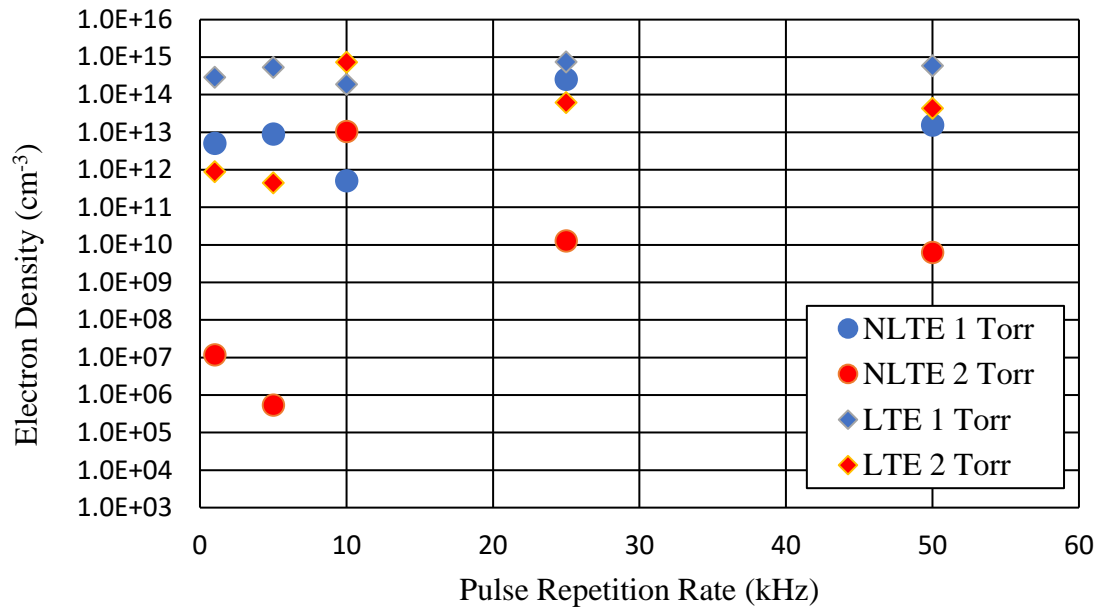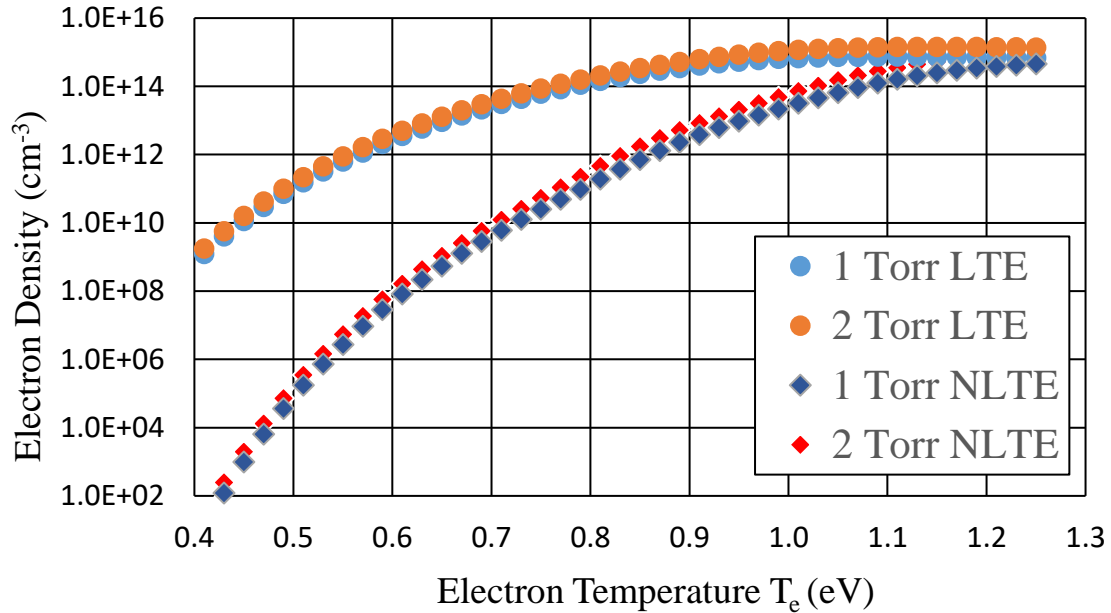

FIGURE 38 – Diagram depicts the calculated electron number density as a function of electron temperatures and PrismSPECT with LTE and Non-LTE assumptions for argon.

The estimated errors contribution due to the intensity measurement of the transitions are small. If we assume shot noise limited measurements and the 20 spectrum measurements taken at each condition are independent, the error of the intensities are less than 2.5% in the smallest signal case. The typical error associated with most of the intensities are less than 1%. Most of the atomic constants used in the calculation are also known to high precision [32]. The atomic constant with the highest uncertainty is the transition probability with has a listed accuracy of $\leq 25\%$. This constant and the energy range of the argon atomic transitions I sample drive the uncertainty in the electron temperature calculation. This uncertainty leads to a large uncertainty in the estimation of

the electron number density. In addition, any large deviations of the data points from the fit most likely arise due to the assumptions in our model. As a result of these two factors, only an order of magnitude estimate of the electron density can be made. Since the integration time of the spectra is much longer than an individual pulse, this calculated value of electron temperature and electron number density can only be considered an estimate. Future work should be targeted toward getting a time-resolved electron temperature and density value.

The dependence of the electron temperature with the number of pulses the average atom experiences can be estimated to see if there is a scaling law relationship. The residence time τ of an atom in the electrode discharge region is estimated by the mass of the system m_s divided by the mass flow rate f_m.

$$\tau = \frac{m_s}{f_m} \tag{16}$$

In our case, we have 1-Torr and 2-Torr argon which we assume for this calculation is 300 K. We set the gas flow to be constant in both cases at 20 sccm (N_2). Using the given gas correction factors from the mass flow regulator manual, we see that the flow rate is approximately 14.39 sccm (Ar). This flow rate results in a mass flow rate of approximately 4.3×10^{-7} kg/s. We consider the gas in the electrode as an ideal gas to calculate the number density and use that number density to calculate the m_s. Combining these two calculated values, we obtain a residence time of approximately 25 ms (1-Torr case) and 50 ms (2-Torr case). The residence time is higher in the 2-Torr case since we keep the mass flow constant but throttle down the vacuum pump using the regulation valve. Using the residence time and pulse repetition rate, we can estimate the number of discharge pulses an atom

experiences while inside the discharge electrode region. The electron temperature normalized with respect to the number of experienced pulses and number of pulses if plotted in Figure 39. Ideally, if the electron density scales with electron temperature, we would like to operate near the knee of this curve where the product is maximized. However, the number of pulses will increase as we increase the duty cycle of the antenna to radiate efficiently. This implies the region we will operate will be starting from the knee to a place to be determined farther along the x-axis of Figure 39.
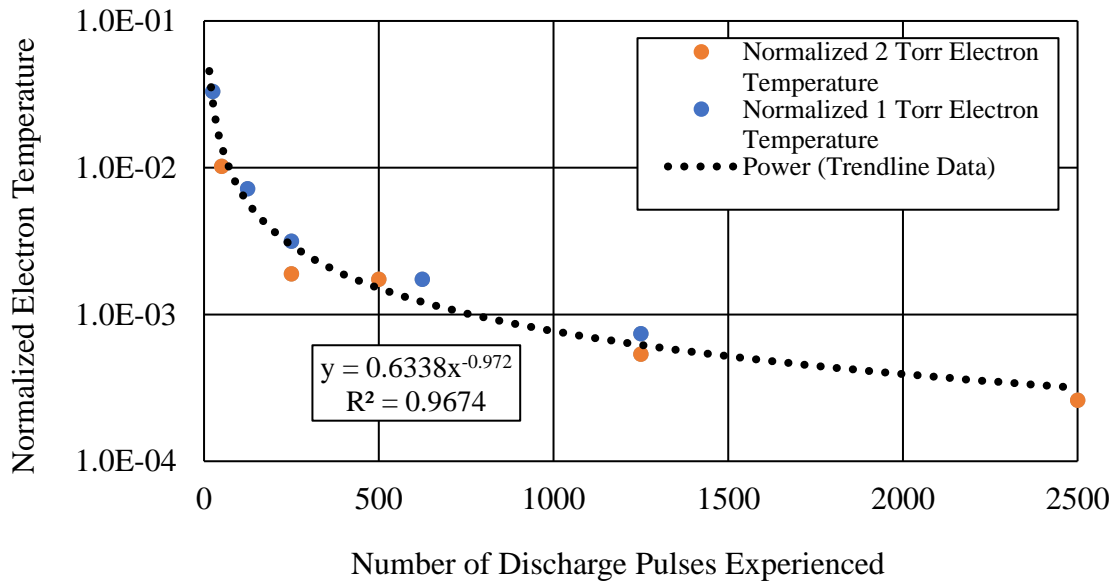
Figure 39 – This plot illustrates the normalized electron temperature (with respect to the number of discharge pulses experienced for an average atom crossing the discharge region) as a function of the number of discharge pulses experienced. We see the 1-Torr and 2-Torr cases follow a power law relationship between these two variables. The number of discharge pulses is calculated using the residence time for the given discharge condition divided by the pulse repetition rate for the given discharge condition.

Adamovich *et al*. analysed the energy coupling to plasma driven by repetitive nanosecond pulse discharges. Similar to his conclusions, the cause for the drop in normalized electron temperature with the increase in the number of discharge pulses is

attributed to the energy coupling at the beginning of the voltage pulse [39]. As the number of discharge pulses an atom experiences increases, the probability the outermost electron occupying metastable states increases. Consequently, the gas inside the discharge region becomes requires lower energy to ionize. At the beginning of a pulse, the increase of discharge pulse rate results in an increase in the rate of rise of the electron density. This faster electron density increase will tend to shield the applied field faster as well. With the applied field shielded faster, the electron heating in the bulk plasma becomes limited for the rest of the pulse duration. This explains the observation of a slower rate of increase in electron temperature decrease despite dramatically increasing the discharge pulse number. In their paper, Adamovich *et al.* argues that to increase energy coupling efficiency in dielectric breakdown discharges, shorter pulse durations and higher voltages are required [39]. In our situation, the rest of the energy of the pulse that does not go into heating the plasma is diverted to our voltage divider circuit. This voltage divider circuit is connected in parallel to the discharge electrodes. Future work to verify this conclusion include decreasing the pulse duration or increasing the applied voltage. For the same gas conditions, the normalized electron temperature curve should have a smaller power law (i.e., the exponent should be raised to a power greater than -0.972). Either change should make the heating of the plasma more effective.

An additional parameter that should be obtained is the temperature of the heavy species (ions and neutrals), this can be obtained with a Doppler measurement of emission lines once a higher resolution (approximately 0.05 nm resolution) spectrometer or monochromator is setup. This parameter is used in both PrismSPECT and presumably other models as an input condition.

Lastly, a source of error that is harder to quantify is the light emission inhomogeneity due to localized enhanced discharge areas. These areas form near the electrode where the anodized layer is thinner than nominal. These enhanced discharge areas are very bright due to higher electron densities and may weigh the measured emissions to the higher end of the electron densities. This situation seems to more likely occur at the high pulse repetition rates. Refer to Figure 39 for a comparison of the 2-Torr case at 1 kHz and 50 kHz pulse repetition rate. Future work to address this issue may include increasing the anodization layer of the electrodes and further changing the geometry of the electrode to reduce any places that may enhance the electric field of the electrodes.
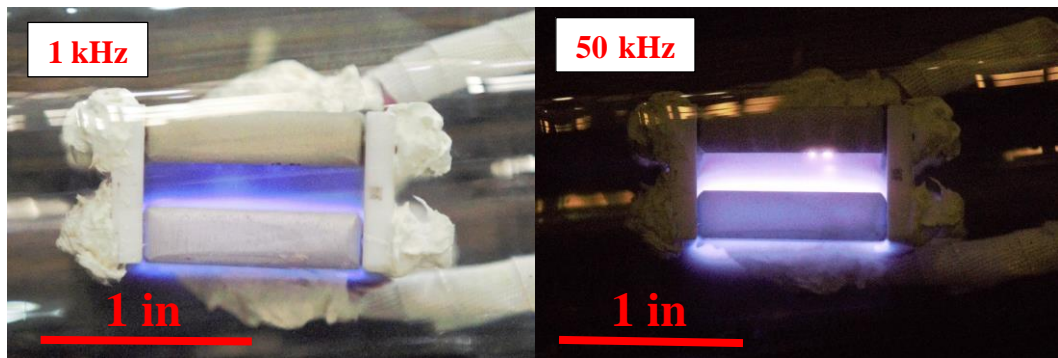

Figure 40 – The pictures depict the 1-kHz case (left) and the 50-kHz case (right) for a 2-Torr argon discharge at 1-kV, 50-ns pulse duration. Note the localized brighter spots and area around the electrodes are more prominent in the 50-kHz case.

CONCLUSIONS

Using the photodiode data, we can conclude the plasma ignition does occur on the time scales (< 11 ns) we would like to achieve. The light curve measurement represents a conservative estimate of the timing for peak electron densities. I also discovered that our measured pulser rise time is slower than specified on the data sheet. The discharge circuit is suspected of slowing down the rise time down from approximately 1.5 ns to ~10 ns. Further investigation into optimization of the circuit is necessary to ensure the voltage rise is not the limiting factor for plasma ignition.

From the plasma spectroscopy measurement, we determined an estimate of the electron temperature (Boltzmann plots) and electron density (with the help of PrismSPECT). The error of these calculations was primarily driven by the uncertainty in the transition probabilities of the emission lines used for the analysis. Within the error of our estimate there is no strong dependence of electron temperature with pulse repetition rate. The calculated electron density with the non-LTE assumption was calculated using PrismSPECT to be in the range of 10^6 to 10^{14} cm^{-3}. The higher end of the estimated electron density range is sufficient for the VAIPER antenna scheme to work if the amplitude modulation is of order 1 GHz or slower. We suspect the values of the higher electron densities calculated for the high pulse repetition rates (>10 kHz) can be skewed due to light emissions from locally enhanced discharge spots. Work should be performed to reduce these spots discharges and a re-measurement should be performed to see if these spots are the cause for the higher values. We also found a power law that relates the calculated

electron temperature (normalized to an estimated, average number of pulses an atom experiences) to the estimated, average number of pulses an atom experiences.

The electrical data collection setup I described represents the most optimum corner in terms of voltage and bandwidth performance that I could commercially obtain. Before attempting to further increase the performance frontier of the instrumentation, it is worthwhile to investigate speeding up the rising edge of the voltage pulse closer to the manufacturer specification as much as possible. An effort should also be made to reduce the reflections due to impedance mismatches that occur through the pulse. Each nanosecond pulser is quite expensive and the premium the lab pays in terms of fast rise times is lost if the rest of the discharge circuit slows and disperses this even before the plasma is ignited. Lastly, through this research, a new aspect of the plasma ignition needs to also be clarified. If the delay in plasma ignition is sensitive to discharge conditions, it needs to be better characterized to achieve the correct pulse timing for multiple cells.

REFERENCES

[1] Jackson, John David. *Classical Electrodynamics*. 3rd ed. New York, NY: Wiley, 1999.

[2] Miligan, Thomas. Modern Antenna Design 2nd Edition, John Wiley and Sons, Inc., New Jersey, 2005.

[3] E. Norris, T. Anderson, and I. Alexeff, "Reconfigurable Plasma Antenna," Patent number 6,369,763, April 9, 2002.

[4] Anderson, Theodore. Plasma antennas. Artech house, 2011.

[5] Borg, G. G., et al. "Plasmas as antennas: Theory, experiment and applications," Physics of Plasmas (1994-present)7.5 (2000): 2198-2202.

[6] Borg, G. G., et al. "Application of plasma columns to radiofrequency antennas," Applied Physics Letters 74.22 (1999): 3272-3274.

[7] Jenn, D. C., "Plasma Antennas: Survey of Techniques and the Current State of the Art," Naval Postgraduate School, published 2003-09-29, accessed 2016-09-15.

[8] Hutchinson, Ian H. "Principles of plasma diagnostics." Plasma Physics and Controlled Fusion 44.12 (2002): 2603.

[9] Kunze, Hans-Joachim. *Introduction to plasma spectroscopy*. Vol. 56. Springer Science & Business Media, 2009.

[10] Griem, Hans R. Principles of plasma spectroscopy. Vol. 2. Cambridge University Press, 2005.

[11] Wamsley, R. C., K. Mitsuhashi, and J. E. Lawler. "High sensitivity absorption spectroscopy in glow discharge plasmas." Review of scientific instruments 64.1 (1993): 45-48.

[12] Cunge, G., et al. "Broadband and time-resolved absorption spectroscopy with light emitting diodes: Application to etching plasma monitoring." Applied Physics Letters 91.23 (2007): 231503.

[13] Vempaire, D., and G. Cunge. "Probing radical kinetics in the afterglow of pulsed discharges by absorption spectroscopy with light emitting diodes: Application to BCl radical." Applied Physics Letters 94.2 (2009): 021504.

[14] Hart, L. P., B. W. Smith, and N. Omenetto. "Evaluation of argon metastable number densities in the inductively coupled plasma by continuum source absorption spectrometry." Spectrochimica Acta Part B: Atomic Spectroscopy 41.12 (1986): 1367-1380.

[15] Manoharan, R., P. L. Varghese, and S. O'Byrne. "Plasma diagnostics of a DC glow discharge using Tuneable Diode Laser Absorption Spectroscopy." (2014).

[16] Uchida, Hiroshi, et al. "Measurement of metastable argon in an inductively coupled argon plasma by atomic absorption spectroscopy." Spectrochimica Acta Part B: Atomic Spectroscopy 35.11-12 (1980): 881-883.

[17] Nikolić, M., et al. "Measurements of population densities of metastable and resonant levels of argon using laser induced fluorescence." Journal of Applied Physics 117.2 (2015): 023304.

[18] Compton, Arthur H. (May 1923). "A Quantum Theory of the Scattering of X-Rays by Light Elements" Physical Review. 21 (5): 483–502.

[19] Bowden, M. D., et al. "A Thomson scattering diagnostic system for measurement of electron properties of processing plasmas." Plasma Sources Science and Technology 8.2 (1999): 203.

[20] Muraoka, K., K. Uchino, and M. D. Bowden. "Diagnostics of low-density glow discharge plasmas using Thomson scattering." Plasma physics and controlled fusion 40.7 (1998): 1221.

[21] ElSabbagh, Mansour A. Mansour, et al. "A laser Thomson scattering system for low density glow discharge plasmas." Japanese Journal of Applied Physics 40.3R (2001): 1465.

[22] Bowden, Mark D., et al. "Detection limit of laser Thomson scattering for low density discharge plasmas." Japanese journal of applied physics 38.6R (1999): 3723.

[23] Heald, Mark A., and Charles B. Wharton. "Plasma diagnostics with microwaves." (1965).

[24] Shneider, Mikhail N., and Richard B. Miles. "Microwave diagnostics of small plasma objects." Journal of Applied Physics 98.3 (2005): 033301.

[25] Park, H., et al. "Recent advancements in microwave imaging plasma diagnostics." Review of scientific instruments 74.10 (2003): 4239-4262.

[26] Neumann, G., et al. "Plasma-density measurements by microwave interferometry and Langmuir probes in an RF discharge." Review of scientific instruments 64.1 (1993): 19-25.

[27] Weber, B. V., and D. D. Hinshelwood. "He–Ne interferometer for density measurements in plasma opening switch experiments." Review of scientific instruments 63.10 (1992): 5199-5201.

[28] Luhmann Jr, N. C. "Instrumentation and techniques for plasma diagnostics: an overview." Infrared and Millimeter Waves 2 (2014).

[29] Bye, Cheryl A., and Alexander Scheeline. "Saha-Boltzmann statistics fordetermination of electron temperature and density in spark discharges using an Echelle/CCD system." Applied Spectroscopy 47.12 (1993): 2022-2030.

[30] J.A Aguilera, C. Aragón, "Characterization of a laser-induced plasma by spatially resolved spectroscopy of neutral atom and ion emissions.: Comparison of local and spatially integrated measurements," Spectrochimica Acta Part B: Atomic Spectroscopy, Volume 59, Issue 12, 2004, Pages 1861-1876.

[31] Palmero, A., et al. "Characterization of a low-pressure argon plasma using optical emission spectroscopy and a global model." Journal of Applied Physics 101.5 (2007): 053306.

[32] Kramida, A., Ralchenko, Yu., Reader, J., and NIST ASD Team (2017). NIST Atomic Spectra Database (ver. 5.5.1), [Online]. Available: https://physics.nist.gov/asd [2017, November 20]. National Institute of Standards and Technology, Gaithersburg, MD.

[33] Ellett, A., and R. M. Zabel. "The Pirani gauge for the measurement of small changes of pressure." Physical Review 37.9 (1931): 1102.

[34] Kurt J. Lesker Company. (2017). 275 Series Convection Vacuum Gauge User Manual. Jefferson Hills, PA: Kurt J. Lesker Company.

[35] FID GmbH. (2016). FPG 1-50NM100A Operation Manual. Burbach, Germany: FID GmbH.

[35] Ocean Optics, Inc. (2008). HR4000 and HR4000CG-UV-NIR Series Spectrometers: Installation and Operation Manual. Dunedin, FL: Ocean Optics, Inc.

[36] Ocean Optics, Inc. (2017). HG-1 Mercury Argon Calibration Light Source: Installation and Operation Instructions. Dunedin, FL: Ocean Optics, Inc.

[37] Corning, Inc. (2017). Properties of PYREX, PYREXPLUS and Low Actinic PYREX Code 7740 Glasses. Corning, NY: Corning, Inc.

[38] Erwin G. Loewen and Evgeny Popov. *Diffraction Gratings and Applications.* CRC Press, 1997.

[39] Adamovich, Igor V., et al. "Energy coupling to the plasma in repetitive nanosecond pulse discharges." Physics of Plasmas 16.11 (2009): 113505.